Article

Cell

A Deep Learning Approach to Antibiotic Discovery

Graphical Abstract

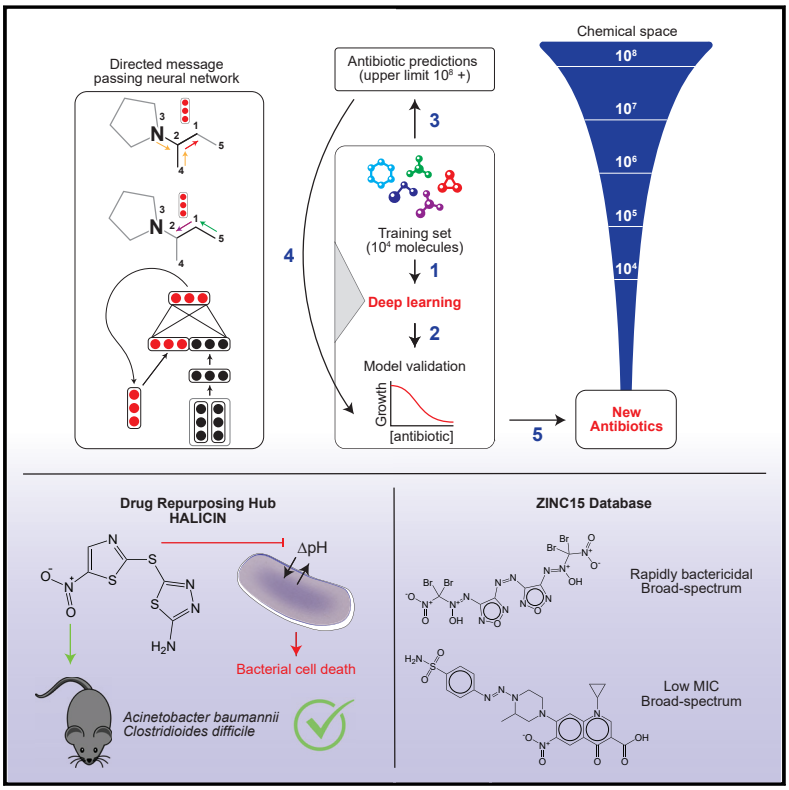

Highlights

- A deep learning model is trained to predict antibiotics based on structure
- Halicin is predicted as an antibacterial molecule from the Drug Repurposing Hub
- Halicin shows broad-spectrum antibiotic activities in mice
- More antibiotics with distinct structures are predicted from the ZINC15 database

Authors

Jonathan M. Stokes, Kevin Yang, Kyle Swanson, ..., Tommi S. Jaakkola, Regina Barzilay, James J. Collins

Correspondence

regina@csail.mit.edu (R.B.), jimjc@mit.edu (J.J.C.)

In Brief

A trained deep neural network predicts antibiotic activity in molecules that are structurally different from known antibiotics, among which Halicin exhibits efficacy against broad-spectrum bacterial infections in mice.

Stokes et al., 2020, Cell *180*, 688–702
February 20, 2020
https://doi.org/10.1016/j.cell.2020.01.021

CellPress

Cell

Article

A Deep Learning Approach to Antibiotic Discovery

Jonathan M. Stokes,[1,2,3] Kevin Yang,[3,4,10] Kyle Swanson,[3,4,10] Wengong Jin,[3,4] Andres Cubillos-Ruiz,[1,2,5] Nina M. Donghia,[1,5] Craig R. MacNair,[6] Shawn French,[6] Lindsey A. Carfrae,[6] Zohar Bloom-Ackerman,[2,7] Victoria M. Tran,[2] Anush Chiappino-Pepe,[5,7] Ahmed H. Badran,[2] Ian W. Andrews,[1,2,5] Emma J. Chory,[1,2] George M. Church,[5,7,8] Eric D. Brown,[6] Tommi S. Jaakkola,[3,4] Regina Barzilay,[3,4,9,*] and James J. Collins[1,2,5,8,9,11,*]

[1]Department of Biological Engineering, Synthetic Biology Center, Institute for Medical Engineering and Science, Massachusetts Institute of Technology, Cambridge, MA 02139, USA

[2]Broad Institute of MIT and Harvard, Cambridge, MA 02142, USA

[3]Machine Learning for Pharmaceutical Discovery and Synthesis Consortium, Massachusetts Institute of Technology, Cambridge, MA 02139, USA

[4]Computer Science and Artificial Intelligence Laboratory, Massachusetts Institute of Technology, Cambridge, MA 02139, USA

[5]Wyss Institute for Biologically Inspired Engineering, Harvard University, Boston, MA 02115, USA

[6]Department of Biochemistry and Biomedical Sciences, Michael G. DeGroote Institute for Infectious Disease Research, McMaster University, Hamilton, ON L8N 3Z5, Canada

[7]Department of Genetics, Harvard Medical School, Boston, MA 02115, USA

[8]Harvard-MIT Program in Health Sciences and Technology, Cambridge, MA 02139, USA

[9]Abdul Latif Jameel Clinic for Machine Learning in Health, Massachusetts Institute of Technology, Cambridge, MA 02139, USA

[10]These authors contributed equally

[11]Lead Contact

*Correspondence: regina@csail.mit.edu (R.B.), jimjc@mit.edu (J.J.C.)

https://doi.org/10.1016/j.cell.2020.01.021

SUMMARY

Due to the rapid emergence of antibiotic-resistant bacteria, there is a growing need to discover new antibiotics. To address this challenge, we trained a deep neural network capable of predicting molecules with antibacterial activity. We performed predictions on multiple chemical libraries and discovered a molecule from the Drug Repurposing Hub—halicin—that is structurally divergent from conventional antibiotics and displays bactericidal activity against a wide phylogenetic spectrum of pathogens including *Mycobacterium tuberculosis* and carbapenem-resistant Enterobacteriaceae. Halicin also effectively treated *Clostridioides difficile* and pan-resistant *Acinetobacter baumannii* infections in murine models. Additionally, from a discrete set of 23 empirically tested predictions from >107 million molecules curated from the ZINC15 database, our model identified eight antibacterial compounds that are structurally distant from known antibiotics. This work highlights the utility of deep learning approaches to expand our antibiotic arsenal through the discovery of structurally distinct antibacterial molecules.

INTRODUCTION

Since the discovery of penicillin, antibiotics have become the cornerstone of modern medicine. However, the continued efficacy of these essential drugs is uncertain due to the global dissemination of antibiotic-resistance determinants. Moreover, the decreasing development of new antibiotics in the private sector that has resulted from a lack of economic incentives is exacerbating this already dire problem (Brown and Wright, 2016; PEW Trusts, 2019). Indeed, without immediate action to discover and develop new antibiotics, it is projected that deaths attributable to resistant infections will reach 10 million per year by 2050 (O'Neill, 2014).

Historically, antibiotics were discovered largely through screening soil-dwelling microbes for secondary metabolites that prevented the growth of pathogenic bacteria (Clardy et al., 2006; Wright, 2017). This approach resulted in the majority of clinically used classes of antibiotics, including β-lactams, aminoglycosides, polymyxins, and glycopeptides, among others. Semi-synthetic derivatives of these scaffolds have maintained a viable clinical arsenal of antibiotics by increasing potency, decreasing toxicity, and sidestepping resistance determinants. Entirely synthetic antibiotics of the pyrimidine, quinolone, oxazolidinone, and sulfa classes have also found prolonged clinical utility, and continue to be optimized for the same properties.

Unfortunately, the discovery of new antibiotics is becoming increasingly difficult. Natural product discovery is now plagued by the dereplication problem, wherein the same molecules are being repeatedly discovered (Cox et al., 2017). Moreover, given the rapid expansion of chemical spaces that are accessible by the derivatization of complex scaffolds (Ortholand and Ganesan, 2004), engineering next-generation versions of existing antibiotics results in substantially more failures than leads. Therefore, many antibiotic discovery programs have turned to screening large synthetic chemical libraries (Tommasi et al., 2015). However, these libraries, which can contain hundreds of thousands

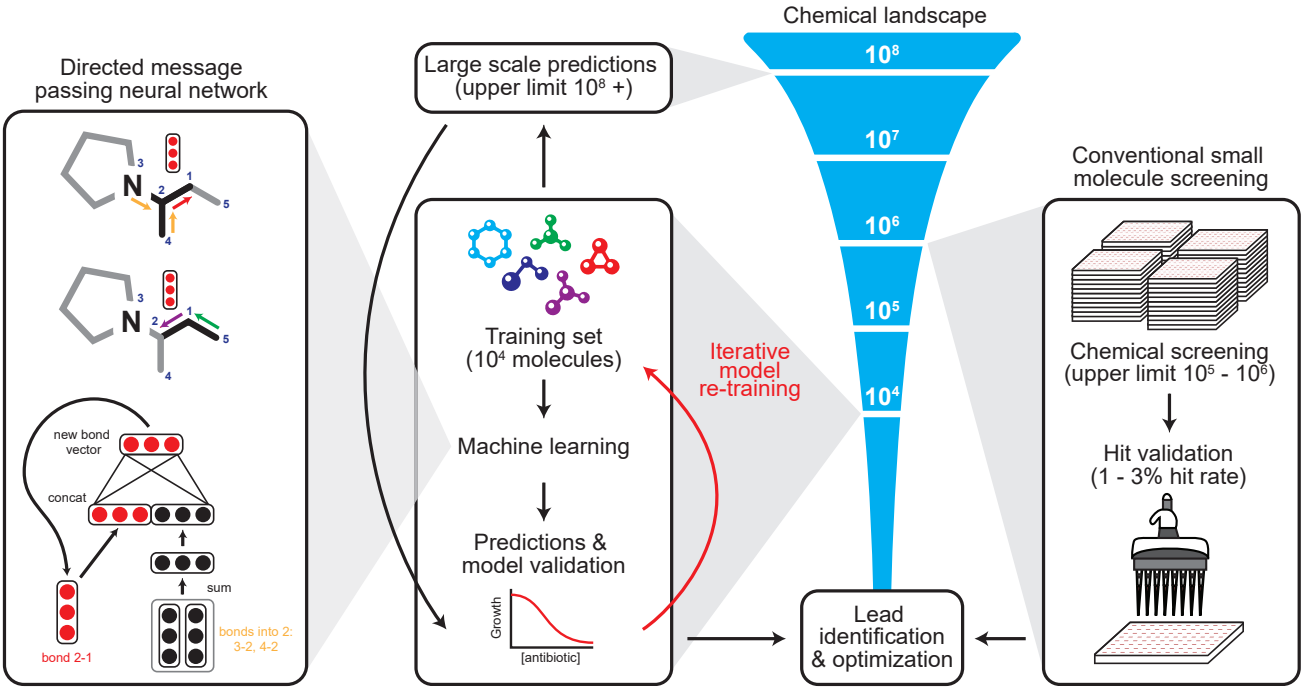

Figure 1. Machine Learning in Antibiotic Discovery

Modern approaches to antibiotic discovery often include screening large chemical libraries for those that elicit a phenotype of interest. These screens, which are upper bound by hundreds of thousands to a few million molecules, are expensive, time consuming, and can fail to capture an expansive breadth of chemical space. In contrast, machine learning approaches afford the opportunity to rapidly and inexpensively explore vast chemical spaces *in silico*. Our deep neural network model works by building a molecular representation based on a specific property, in our case the inhibition of the growth of *E. coli*, using a directed message passing approach. We first trained our neural network model using a collection of 2,335 diverse molecules for those that inhibited the growth of *E. coli*, augmenting the model with a set of molecular features, hyperparameter optimization, and ensembling. Next, we applied the model to multiple chemical libraries, comprising >107 million molecules, to identify potential lead compounds with activity against *E. coli*. After ranking the candidates according to the model's predicted score, we selected a list of promising candidates.

to a few million molecules, are often prohibitively costly to curate, limited in chemical diversity, and fail to reflect the chemistry that is inherent to antibiotic molecules (Brown et al., 2014). Since the implementation of high-throughput screening in the 1980s, no new clinical antibiotics have been discovered using this method.

Novel approaches to antibiotic discovery are needed to increase the rate at which new antibiotics are identified and simultaneously decrease the associated cost of early lead discovery. Given recent advancements in machine learning (Camacho et al., 2018), the field is now ripe for the application of algorithmic solutions for molecular property prediction to identify novel structural classes of antibiotics. Indeed, adopting methodologies that allow early drug discovery to be performed largely *in silico* enables the exploration of vast chemical spaces that is beyond the reach of current experimental approaches.

The idea of analytical exploration in drug design is not new. Decades of prior work in chemoinformatics have developed models for molecular property prediction (Mayr et al., 2018; Wu et al., 2017). However, the accuracy of these models has been insufficient to substantially change the traditional drug discovery pipeline. With recent algorithmic advancements in modeling neural network-based molecular representations, we are beginning to have the opportunity to influence the paradigm of drug discovery. An important development relates to how molecules are represented; traditionally, molecules were represented by their fingerprint vectors, which reflected the presence or absence of functional groups in the molecule, or by descriptors that include computable molecular properties and require expert knowledge to construct (Mauri et al., 2006; Moriwaki et al., 2018; Rogers and Hahn, 2010). Even though the mapping from these representations to properties was learned automatically, the fingerprints and descriptors themselves were designed manually. The innovation of neural network approaches lies in their ability to learn this representation automatically, mapping molecules into continuous vectors that are subsequently used to predict their properties. These designs result in molecular representations that are highly attuned to the desired property, yielding gains in property prediction accuracy over manually crafted representations (Yang et al., 2019b).

While neural network models narrowed the performance gap between analytical and experimental approaches, a difference still exists. Here, we demonstrate how the combination of *in silico* predictions and empirical investigations can lead to the discovery of new antibiotics (Figure 1). Our approach consists of three stages. First, we trained a deep neural network model to predict growth inhibition of *Escherichia coli* using a collection of 2,335 molecules. Second, we applied the resulting

model to several discrete chemical libraries, comprising >107 million molecules, to identify potential lead compounds with activity against *E. coli*. After ranking the compounds according to the model's predicted score, we lastly selected a list of candidates based on a pre-specified prediction score threshold, chemical structure, and availability.

Through this approach, from the Drug Repurposing Hub, we identified the c-Jun N-terminal kinase inhibitor SU3327 (De et al., 2009; Jang et al., 2015) (renamed halicin herein), which is structurally divergent from conventional antibiotics, as a potent inhibitor of *E. coli* growth. Further investigations revealed that halicin displays growth inhibitory properties against a wide phylogenetic spectrum of pathogens through selective dissipation of the bacterial transmembrane ΔpH potential. Importantly, halicin shows efficacy against *Clostridioides difficile* and pan-resistant *Acinetobacter baumannii* infections in murine models. Of note, the World Health Organization has designated *A. baumannii* as one of the highest priority pathogens against which new antibiotics are urgently required (Lee et al., 2017; Perez et al., 2007). In addition to halicin, from a distinct set of 23 empirically tested predictions from >107 million molecules found in the ZINC15 database, we readily discovered eight additional antibacterial compounds that are structurally distant from known antibiotics. Remarkably, two of these molecules displayed potent broad-spectrum activity and could overcome an array of antibiotic-resistance determinants in *E. coli*. This work highlights the significant impact that machine learning can have on early antibiotic discovery efforts by simultaneously increasing the accuracy rate of lead compound identification and decreasing the cost of screening efforts.

RESULTS

Initial Model Training and the Identification of Halicin

Initially, we desired to obtain a training dataset *de novo* that was inexpensive, chemically diverse, and did not require sophisticated laboratory resources. This would allow for the development of a robust model with which new antibiotics could be predicted, without the practical hurdles that can be associated with large-scale antibiotic screening efforts. We screened for growth inhibition against *E. coli* BW25113 (Zampieri et al., 2017) using a widely available US Food and Drug Administration (FDA)-approved drug library consisting of 1,760 molecules of diverse structure and function. To further increase chemical diversity, we included an additional 800 natural products isolated from plant, animal, and microbial sources, resulting in a primary training set of 2,560 molecules (Figures 2A and S1A; Table S1A)—2,335 unique compounds when deduplicated (Figure S1B; Table S1B). Using 80% growth inhibition as a hit cut-off, this primary screen resulted in the identification of 120 molecules with growth inhibitory activity against *E. coli*.

Next, all 2,335 compounds from the primary training dataset were binarized as hit or non-hit. After binarization, we used these data to train a binary classification model that predicts the probability of whether a new compound will inhibit the growth of *E. coli* based on its structure. For this purpose, we utilized a directed-message passing deep neural network model (Yang et al., 2019b), which translates the graph representation of a molecule into a continuous vector via a directed bond-based message passing approach. This builds a molecular representation by iteratively aggregating the features of individual atoms and bonds. The model operates by passing "messages" along bonds that encode information about neighboring atoms and bonds. By applying this message passing operation multiple times, the model constructs higher-level bond messages that contain information about larger chemical substructures. The highest-level bond messages are then combined into a single continuous vector representing the entire molecule. Given the limited amount of data available for training the model, it was important to ensure that the model could generalize without overfitting. Therefore, we augmented the learned representation with molecular features computed by RDKit (Landrum, 2006) (Table S2A), yielding a hybrid molecular representation. We further increased the algorithm's robustness by utilizing an ensemble of classifiers and estimating hyperparameters with Bayesian optimization. The resulting model achieved a receiver operating characteristic curve-area under the curve (ROC-AUC) of 0.896 on the test data (Figure 2B).

After model development and optimization using our training dataset of 2,335 molecules, we subsequently applied an ensemble of models trained on twenty folds to identify potential antibacterial molecules from the Drug Repurposing Hub (Corsello et al., 2017). This library consists of 6,111 molecules at various stages of investigation for human diseases. Here, prediction scores for each compound were determined, molecules were ranked based on their probability of displaying growth inhibition against *E. coli*, and compounds with molecular graphs common between the training dataset and the Drug Repurposing Hub were removed (Figure 2C; Table S2B). Notably, we compared the molecule prediction ranks from our model (Table S2B) to numerous others, including a learned model without RDKit feature augmentation (Table S2C), a model trained exclusively on RDKit features (Table S2D), a feed-forward deep neural network model using Morgan fingerprints as the molecular representation (Table S2E), a random forest classifier using Morgan fingerprints (Table S2F), and a support-vector machine model using Morgan fingerprints (Table S2G).

Next, we curated the 99 molecules unique to the Drug Repurposing Hub that were most strongly predicted to display antibacterial properties by our model and empirically tested these for growth inhibition. We observed that 51 of the 99 predicted molecules displayed growth inhibition against *E. coli*, based on a cut-off of OD_{600} <0.2 (Figure 2D). Importantly, higher prediction scores correlated with a greater probability of growth inhibition (Figure 2E). Furthermore, empirically testing the lowest predicted 63 molecules that were unique to the Drug Repurposing Hub revealed that only two of these compounds displayed growth inhibitory activity (Figure 2F).

After identifying the 51 molecules that displayed growth inhibition against *E. coli*, we prioritized these based on clinical phase of investigation, structural similarity to molecules in the primary training dataset, and predicted toxicity using a deep neural network model trained on the ClinTox database (Gayvert et al., 2016; Wu et al., 2017) (Table S2B). Specifically, we prioritized predicted compounds in preclinical or Phase 1/2/3 studies, those with low structural similarity to training set molecules, and

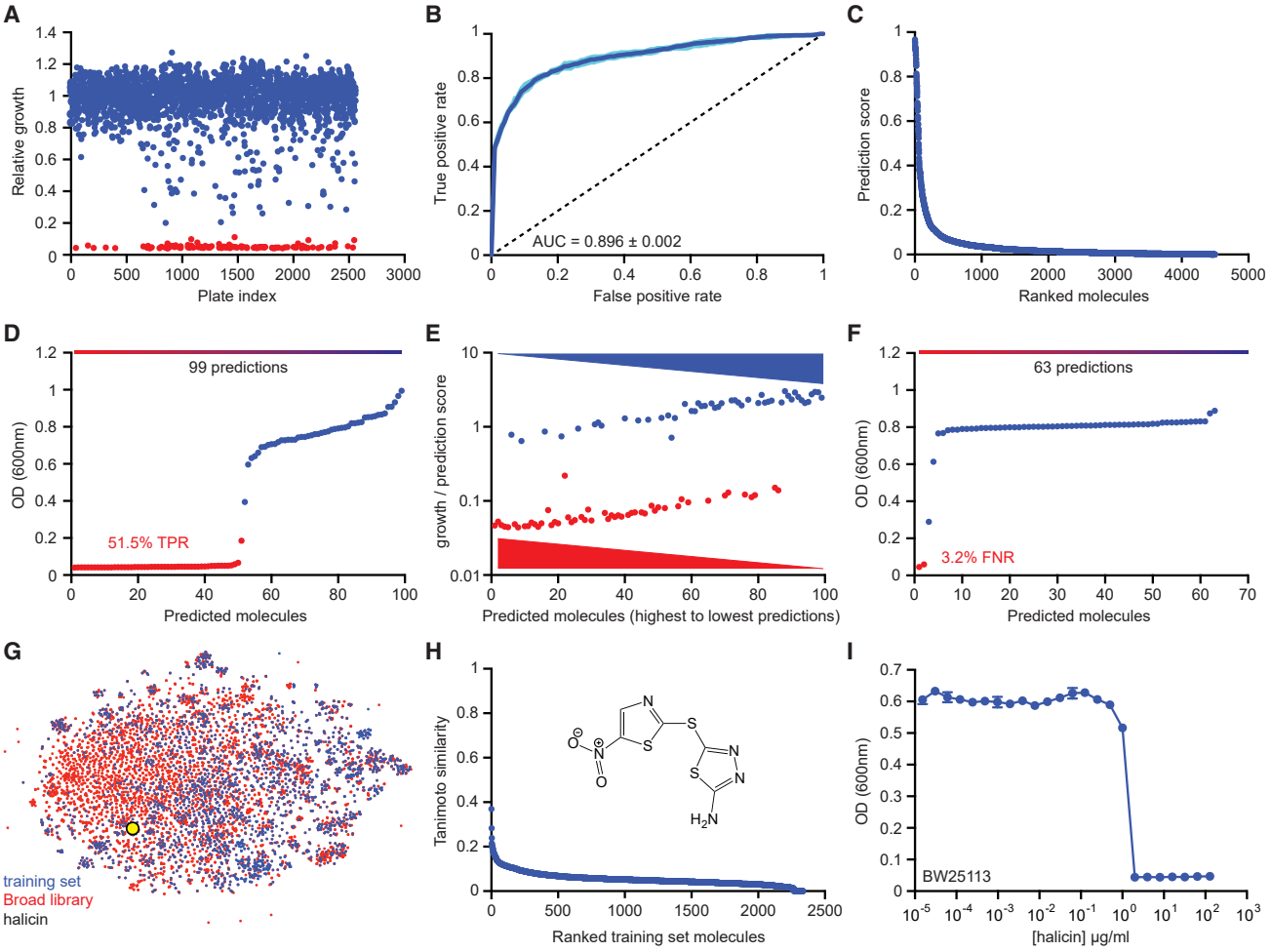

Figure 2. Initial Model Training and the Identification of Halicin

(A) Primary screening data for growth inhibition of *E. coli* by 2,560 molecules within the FDA-approved drug library supplemented with a natural product collection. Shown is the mean of two biological replicates. Red are growth inhibitory molecules; blue are non-growth inhibitory molecules.

(B) ROC-AUC plot evaluating model performance after training. Dark blue is the mean of six individual trials (cyan).

(C) Rank-ordered prediction scores of Drug Repurposing Hub molecules that were not present in the training dataset.

(D) The top 99 predictions from the data shown in (C) were curated for empirical testing for growth inhibition of *E. coli*. Fifty-one of 99 molecules were validated as true positives based on a cut-off of OD_{600} <0.2. Shown is the mean of two biological replicates. Red are growth inhibitory molecules; blue are non-growth inhibitory molecules.

(E) For all molecules shown in (D), ratios of OD_{600} to prediction score were calculated and these values were plotted based on prediction score for each corresponding molecule. These results show that a higher prediction score correlates with a greater probability of growth inhibition.

(F) The bottom 63 predictions from the data shown in (C) were curated for empirical testing for growth inhibition of *E. coli*. Shown is the mean of two biological replicates. Red are growth inhibitory molecules; blue are non-growth inhibitory molecules.

(G) t-Distributed stochastic neighbor embedding (t-SNE) of all molecules from the training dataset (blue) and the Drug Repurposing Hub (red), revealing chemical relationships between these libraries. Halicin is shown as a black and yellow circle.

(H) Tanimoto similarity between halicin (structure inset) and each molecule in the de-duplicated training dataset. The Tanimoto nearest neighbor is the antiprotozoal drug nithiamide (score ~0.37), with metronidazole being the nearest antibiotic (score ~0.21).

(I) Growth inhibition of *E. coli* by halicin. Shown is the mean of two biological replicates. Bars denote absolute error.

See also Figure S1 and Tables S1 and S2.

those with low predicted toxicity. The compound that satisfied all of these criteria was the c-Jun N-terminal kinase inhibitor SU3327 (De et al., 2009; Jang et al., 2015) (renamed halicin), a preclinical nitrothiazole under investigation as a treatment for diabetes. Excitingly, halicin, which is structurally most similar to a family of nitro-containing antiparasitic compounds (Tanimoto similarity ~0.37; Figures 2G and 2H; Table S2H) (Rogers and Hahn, 2010) and the antibiotic metronidazole (Tanimoto similarity ~0.21), displayed excellent growth inhibitory activity against *E. coli*, achieving a minimum inhibitory concentration (MIC) of 2 μg/mL (Figure 2I).

Importantly, we observed that the prediction rank of halicin in our model (position 89) was greater than that in four of the other five models tested (positions ranging from 273 to 1987;

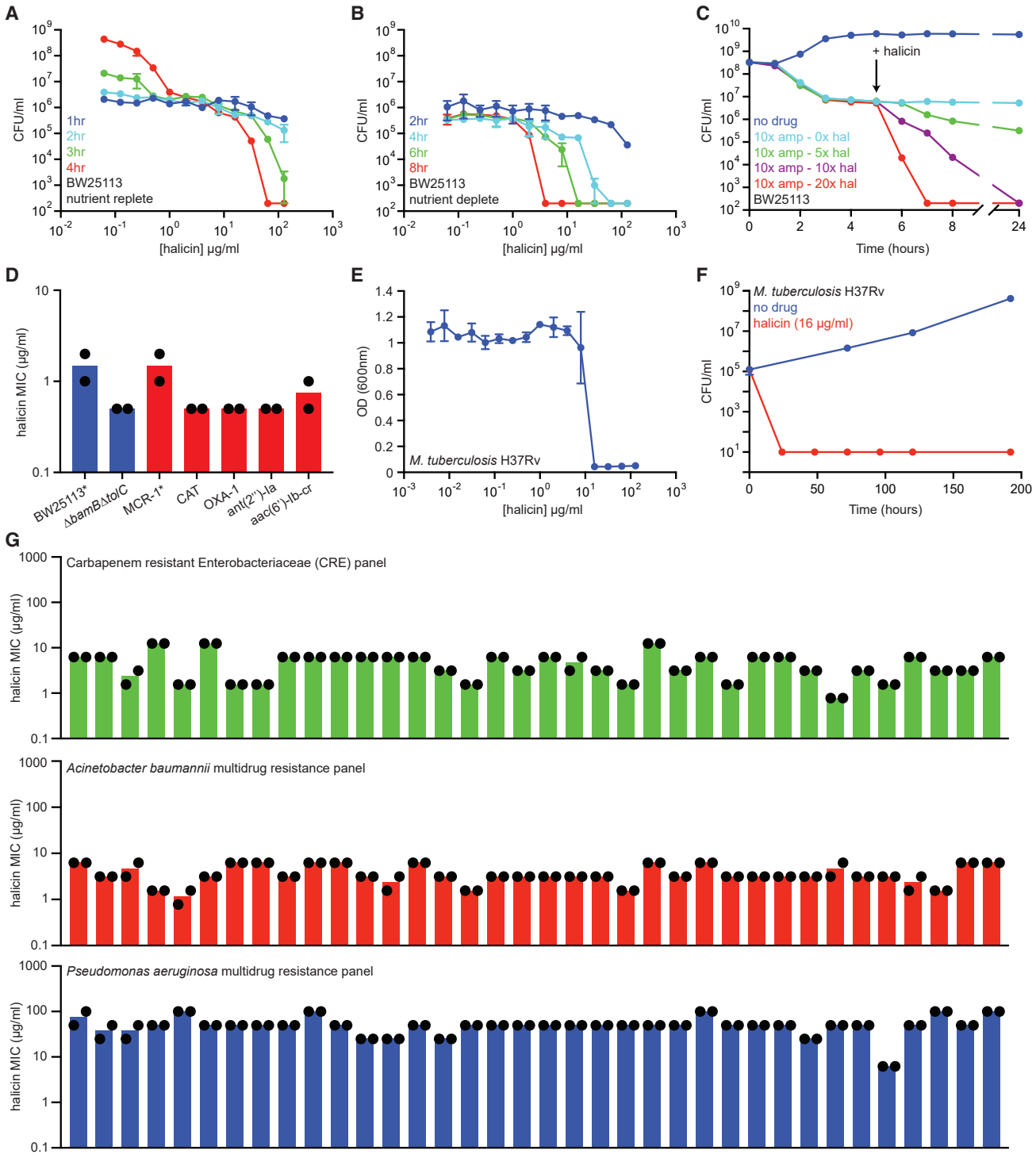

Figure 3. Halicin Is a Broad-Spectrum Bactericidal Antibiotic

(A) Killing of *E. coli* in LB media in the presence of varying concentrations of halicin after 1 h (blue), 2 h (cyan), 3 h (green), and 4 h (red). The initial cell density is ~10^6 CFU/mL. Shown is the mean of two biological replicates. Bars denote absolute error.

(B) Killing of *E. coli* in PBS in the presence of varying concentrations of halicin after 2 h (blue), 4 h (cyan), 6 h (green), and 8 h (red). The initial cell density is ~10^6 CFU/mL. Shown is the mean of two biological replicates. Bars denote absolute error.

(C) Killing of *E. coli* persisters by halicin after treatment with 10 μg/mL (10× MIC) of ampicillin. Light blue is no halicin. Green is 5× MIC halicin. Purple is 10× MIC halicin. Red is 20× MIC halicin. Shown is the mean of two biological replicates. Bars denote absolute error.

(legend continued on next page)

Tables S2D–S2G). Indeed, only the learned model without RDKit augmentation positioned halicin in a higher prediction rank (position 61; Table S2C). These data highlight the importance of using a directed-message passing deep neural network approach in the discovery of halicin.

Halicin Is a Broad-Spectrum Bactericidal Antibiotic

Given that halicin displayed potent growth inhibitory activity against *E. coli*, we next performed time- and concentration-dependent killing assays to determine whether this compound inhibited growth through a bactericidal or bacteriostatic mechanism. In rich growth conditions against an initial cell density of $\sim 10^6$ colony-forming unit (CFU)/mL, we observed bacterial cell killing in the presence of halicin (Figure 3A). The apparent potency of halicin decreased as initial cell density increased (Figures S2A and S2B), likely as a result of dilution of the molecule over a greater number of cells. Next, we considered whether halicin might induce bacterial cell death against *E. coli* in a metabolically repressed, antibiotic-tolerant state (Balaban et al., 2019; Stokes et al., 2019a, 2019b). Indeed, given that metronidazole is bactericidal against non-replicating cells (Tally et al., 1978), we reasoned that halicin may similarly display this activity. Remarkably, by incubating *E. coli* in nutrient-free buffer supplemented with halicin, we observed that this molecule retained bactericidal activity (Figures 3B, S2C, and S2D). This is in stark contrast to the conventionally bactericidal antibiotic ampicillin, which was unable to eradicate *E. coli* existing in metabolically repressed states (Figures S2E–S2G), despite its efficacy against metabolically active cells (Figures S2H–S2J). Moreover, halicin was able to eradicate *E. coli* persister cells that remained after treatment with ampicillin (Figure 3C), consistent with its bactericidal activity against cells in nutrient-free buffer conditions.

The efficacy of halicin against antibiotic-tolerant cells represents a significant improvement over the majority of conventional antibiotics (Lobritz et al., 2015; Stokes et al., 2019b). This observation suggested that the molecule could function through an uncommon mechanism of action, and therefore overcome many common resistance determinants. We initially tested halicin against a selection of *E. coli* strains harboring plasmid-borne antibiotic-resistance genes conferring resistance to polymyxins (MCR-1), chloramphenicol (CAT), β-lactams (OXA-1), aminoglycosides [ant(2″)-Ia], and fluoroquinolones [aac(6′)-Ib-cr]. Here, we observed no change in halicin MIC in the presence of any resistance gene relative to the antibiotic-susceptible parent strains (Figures 3D and S2K). Similarly, the MIC of halicin did not change in *E. coli* displaying resistance to the nitrofuran antibiotic nitrofurantoin via deletion of *nfsA* and *nfsB* (Sandegren et al., 2008) (Figures S2L and S2M).

To more comprehensively assess the ability of halicin to overcome antibiotic-resistance genes, as well as understand phylogenetic spectrum of bioactivity, we assayed for halicin-dependent growth inhibition against *Mycobacterium tuberculosis*, as well as 36 multidrug-resistant clinical isolates each of carbapenem-resistant Enterobacteriaceae (CRE), *A. baumannii*, and *Pseudomonas aeruginosa*. These pathogens are regarded by the World Health Organization as the bacteria that most urgently require new treatments. Excitingly, we observed that halicin was rapidly bactericidal against *M. tuberculosis* (Figures 3E and 3F) and had strong growth inhibitory activity against CRE and *A. baumannii* clinical isolates (Figure 3G; Table S3). While it remains to be experimentally elucidated, the lack of efficacy against *P. aeruginosa* may be explained by insufficient permeability to the cell membrane (Angus et al., 1982; Yoshimura and Nikaido, 1982).

Halicin Dissipates the ΔpH Component of the Proton Motive Force

The observations that halicin retained bactericidal activity against antibiotic-tolerant *E. coli* and *M. tuberculosis*, as well as growth inhibitory properties against multidrug-resistant Gram-negative clinical isolates, suggested that this compound was antibacterial through an unconventional mechanism. Because our model was agnostic to the mechanism of action underlying growth inhibition, we initially attempted to elucidate mechanism through the evolution of halicin-resistant mutants. However, we were unable to isolate spontaneous suppressor mutants after 30 days of serial passaging in liquid media (Figure 4A) or after 7 days of continuous halicin exposure on solid media (Figure S3A). As such, we applied RNA sequencing to understand the physiologic response of *E. coli* to halicin. Here, early-log phase cells were treated with a range of concentrations of compound, and whole-transcriptome sequencing was performed. We observed a rapid downregulation of genes involved in cell motility across all concentrations, as well as the upregulation of genes required for iron homeostasis at sub-lethal concentrations (Figures 4B, S3B, and S3C; Tables S4A–S4C). Interestingly, previous work has shown that dissipation of the cytoplasmic transmembrane potential results in decreased bacterial locomotion and flagellar biosynthesis (Manson et al., 1977; Paul et al., 2008; Shioi et al., 1982). Moreover, given that cells must maintain an electrochemical transmembrane gradient for viability (Hurdle et al., 2011; Coates and Hu, 2008), dissipation of the proton motive force would result in the death of tolerant cells.

To test the hypothesis that halicin dissipated the proton motive force, we first assayed for changes in halicin MIC against *E. coli* as a function of media pH. In *E. coli* (Figure 4C), as well as *Staphylococcus aureus* (Figure S3D), we observed that halicin

(D) MIC of halicin against *E. coli* strains harboring a range of antibiotic-resistance determinants. The *mcr-1* gene was expressed in *E. coli* BW25113. All other resistance genes were expressed in *E. coli* BW25113 Δ*bamB*Δ*tolC*. Experiments were conducted with two biological replicates.
(E) Growth inhibition of *M. tuberculosis* by halicin. Shown is the mean of three biological replicates. Bars denote standard deviation.
(F) Killing of *M. tuberculosis* by halicin in 7H9 media at 16 μg/mL (1× MIC). Shown is the mean of three biological replicates. Bars denote standard deviation.
(G) MIC of halicin against 36-strain panels of CRE isolates (green), *A. baumannii* isolates (red), and *P. aeruginosa* isolates (blue). Experiments were conducted with two biological replicates.
See also Figure S2 and Table S3.

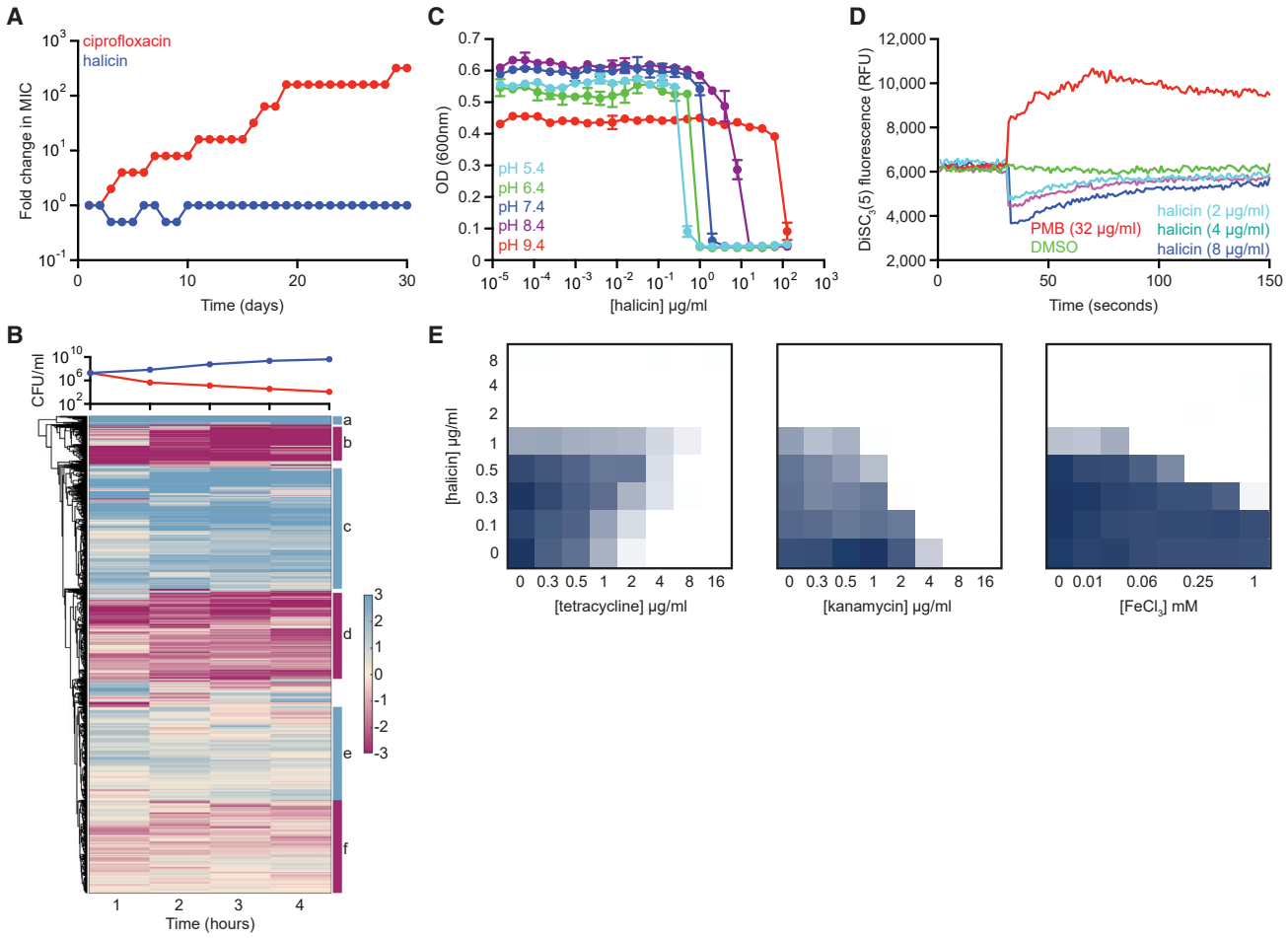

Figure 4. Halicin Dissipates the ΔpH Component of the Proton Motive Force

(A) Evolution of resistance to halicin (blue) or ciprofloxacin (red) in *E. coli* after 30 days of passaging in liquid LB media. Cells were passaged every 24 h.

(B) Whole transcriptome hierarchical clustering of relative gene expression of *E. coli* treated with halicin at 4× MIC for 1 h, 2 h, 3 h, and 4 h. Shown is the mean transcript abundance of two biological replicates of halicin-treated cells relative to untreated control cells on a $\log_2$-fold scale. Genes enriched in cluster b are involved in locomotion ($p\sim10^{-20}$); genes enriched in cluster c are involved in ribosome structure/function ($p\sim10^{-30}$); and genes enriched in cluster d are involved in membrane protein complexes ($p\sim10^{-15}$). Clusters a, e, and f are not highly enriched for specific biological functions. In the growth curve, blue represents untreated cells; red represents halicin-treated cells.

(C) Growth inhibition by halicin against *E. coli* in pH-adjusted media. Shown is the mean of two biological replicates. Bars denote absolute error.

(D) $DiSC_3(5)$ fluorescence in *E. coli* upon exposure to polymyxin B (PMB), halicin, or DMSO.

(E) Growth inhibition checkerboards of halicin in combination with tetracycline (left), kanamycin (center), and $FeCl_3$ (right). Dark blue represents greater growth. See also Figure S3 and Table S4.

potency decreased as pH increased, providing evidence that this compound may be dissipating the ΔpH component of the proton motive force (Farha et al., 2013). Consistent with this observation, the addition of sodium bicarbonate to the growth medium (Farha et al., 2018) antagonized the action of halicin against *E. coli* (Figure S3E).

To further ascertain that halicin dissipates the transmembrane ΔpH potential in bacteria, we applied the potentiometric fluorophore 3,3′-dipropylthiadicarbocyanine iodide [$DiSC_3(5)$] (Wu et al., 1999). $DiSC_3(5)$ accumulates in the cytoplasmic membrane in response to the $\Delta\psi$ component of the proton motive force, and self-quenches its own fluorescence. When $\Delta\psi$ is disrupted, or the membrane is permeabilized, the probe is released into the extracellular milieu resulting in increased fluorescence. Conversely, when ΔpH is disrupted, cells compensate by increasing $\Delta\psi$, resulting in enhanced $DiSC_3(5)$ uptake into the cytoplasmic membrane and therefore decreased fluorescence. Here, early-log *E. coli* cells were washed in buffer and introduced to $DiSC_3(5)$ to allow fluorescence equilibration. Cells were then introduced to polymyxin B (Figure 4D), which disrupts the cytoplasmic membrane, causing release of $DiSC_3(5)$ from the membrane and a corresponding increase in fluorescence. Next, we introduced cells to varying concentrations of halicin, and observed an immediate decrease in $DiSC_3(5)$ fluorescence in a dose-dependent manner (Figure 4D), suggesting that halicin selectively dissipated the ΔpH component of the proton motive

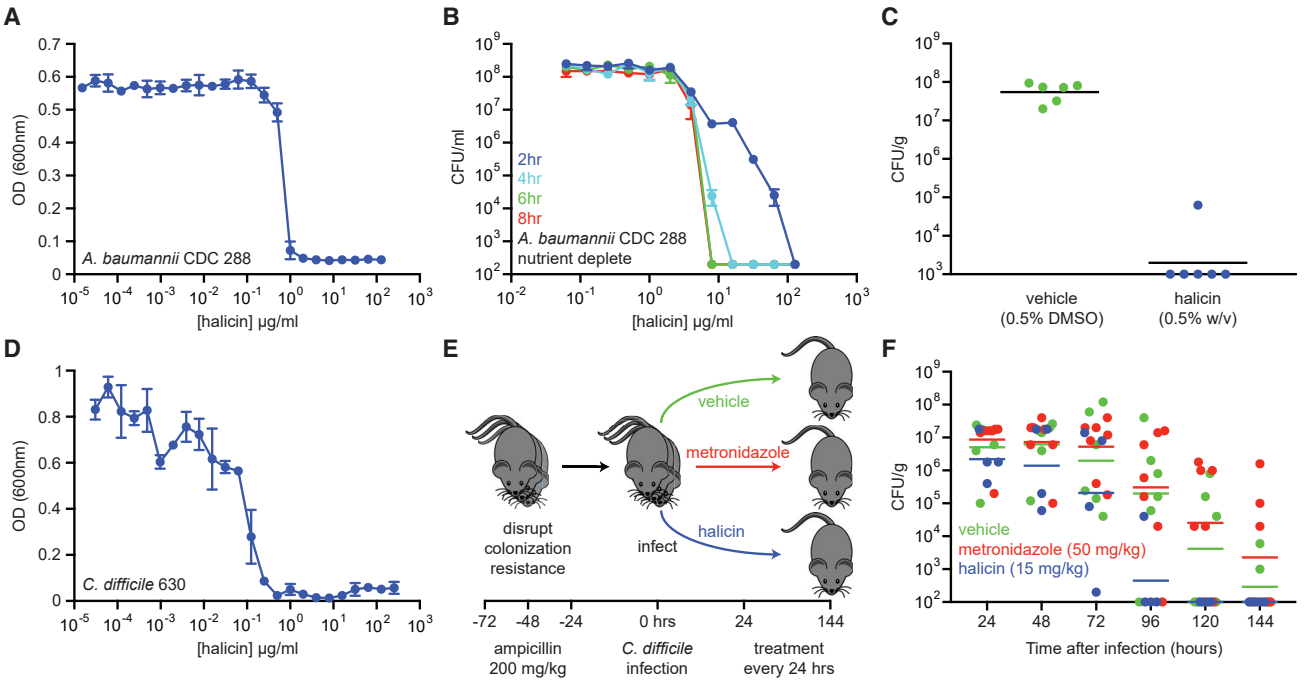

Figure 5. Halicin Displays Efficacy in Murine Models of Infection

(A) Growth inhibition of pan-resistant *A. baumannii* CDC 288 by halicin. Shown is the mean of two biological replicates. Bars denote absolute error.

(B) Killing of *A. baumannii* CDC 288 in PBS in the presence of varying concentrations of halicin after 2 h (blue), 4 h (cyan), 6 h (green), and 8 h (red). The initial cell density is ~10^8 CFU/mL. Shown is the mean of two biological replicates. Bars denote absolute error.

(C) In a wound infection model, mice were infected with *A. baumannii* CDC 288 for 1 h and treated with either vehicle (green; 0.5% DMSO; n = 6) or halicin (blue; 0.5% w/v; n = 6) over 24 h. Bacterial load from wound tissue after treatment was determined by selective plating. Black lines represent geometric mean of the bacterial load for each treatment group.

(D) Growth inhibition of *C. difficile* 630 by halicin. Shown is the mean of two biological replicates. Bars denote absolute error.

(E) Experimental design for *C. difficile* infection and treatment.

(F) Bacterial load of *C. difficile* 630 in feces of infected mice. Metronidazole (red; 50 mg/kg; n = 6) did not result in enhanced rates of clearance relative to vehicle controls (green; 10% PEG 300; n = 7). Halicin-treated mice (blue; 15 mg/kg; n = 4) displayed sterilization beginning at 72 h after treatment, with 100% of mice being free of infection at 96 h after treatment. Lines represent geometric mean of the bacterial load for each treatment group.

See also Figure S4.

force. Similar $DiSC_3(5)$ fluorescence changes were observed in *S. aureus* treated with halicin (Figures S3F and S3G). Moreover, halicin displayed antibiotic antagonism and synergy profiles consistent with ΔpH dissipation. Of note, halicin antagonized the activity of tetracycline in *E. coli*, and synergized with kanamycin (Figure 4E), consistent with previous work showing that the uptake of tetracyclines is dependent upon ΔpH (Yamaguchi et al., 1991), whereas aminoglycoside uptake is driven largely by Δψ (Taber et al., 1987).

Interestingly, our observations that halicin induced the expression of iron acquisition genes at sub-lethal concentrations (Tables S4A–S4C) suggested that this compound complexes with iron in solution, thereby dissipating transmembrane ΔpH potential similarly to other antibacterial ionophores, such as daptomycin (Farha et al., 2013). We note here that daptomycin resistance via deletion of *dsp1* in *S. aureus* did not confer cross-resistance to halicin (Figure S3H). We observed enhanced potency of halicin against *E. coli* with increasing concentrations of environmental Fe^{3+} (Figure 4E). This is consistent with a mechanism of action wherein halicin may bind iron prior to membrane association and ΔpH dissipation.

Halicin Displays Efficacy in Murine Models of Infection

Given that halicin displays broad-spectrum bactericidal activity and is not highly susceptible to plasmid-borne antibiotic-resistance elements or *de novo* resistance mutations at high frequency, we next asked whether this compound might have utility as an antibiotic *in vivo*. We therefore tested the efficacy of halicin in a murine wound model of *A. baumannii* infection. On the dorsal surface of neutropenic BALB/c mice, we established a 2 cm^2 wound and infected with ~2.5 × 10^5 CFU of *A. baumannii* strain 288 acquired from the Centers for Disease Control and Prevention (CDC). This strain is not susceptible to clinical antibiotics generally used for treatment of *A. baumannii*, and therefore represents a pan-resistant isolate. Importantly, halicin displayed potent growth inhibition against this strain *in vitro* (MIC = 1 μg/mL; Figure 5A) and was able to sterilize *A. baumannii* 288 cells residing in metabolically repressed conditions (Figures 5B, S4A, and S4B). After 1 h of infection establishment, mice were treated with Glaxal Base Moisturizing Cream supplemented with vehicle (0.5% DMSO) or halicin (0.5% w/v). Mice were then treated after 4 h, 8 h, 12 h, 20 h, and 24 h of infection, and sacrificed at 25 h

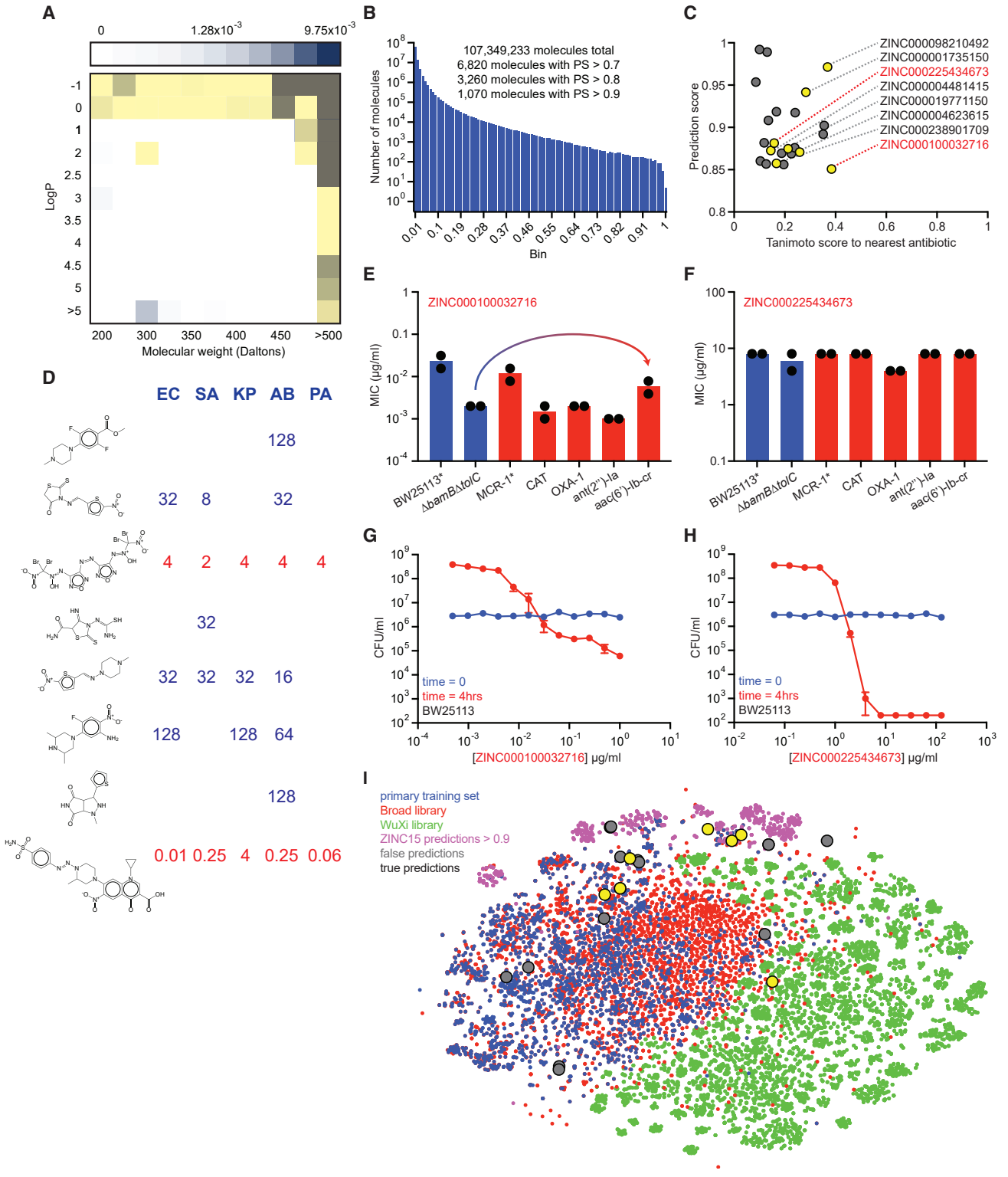

Figure 6. Predicting New Antibiotic Candidates from Unprecedented Chemical Libraries

(A) Tranches of the ZINC15 database colored based on the proportion of hits from the original training dataset of 2,335 molecules within each tranche. Darker blue tranches have a higher proportion of molecules that are growth inhibitory against *E. coli*. Yellow tranches are those selected for predictions.

(B) Histogram showing the number of ZINC15 molecules from selected tranches within a corresponding prediction score range.

(legend continued on next page)

post-infection. We observed that wound-carrying capacity had reached ~10^8 CFU/g in the vehicle control group, whereas 5 of the 6 mice treated with halicin contained <10^3 CFU/g (below the limit of detection) and one contained ~10^5 CFU/g (Figure 5C).

After showing that halicin displayed efficacy against *A. baumannii* in a murine wound model, we next sought to investigate whether this molecule may have utility against a phylogenetically divergent pathogen that is increasingly becoming burdensome to healthcare systems—namely, *C. difficile*. This spore-forming anaerobe causes pseudomembranous colitis, often as a result of dysbiosis following systemic antibiotic administration. Metronidazole or vancomycin are first-line treatments, with failure resulting from antibiotic resistance and/or the presence of metabolically dormant cells (Surawicz et al., 2013). In cases of recurrent infection, fecal bacteriotherapy is required to re-establish the normal colonic microbiota to outcompete *C. difficile* (Gough et al., 2011), which can be more invasive than antibiotic therapy.

We first assayed for the ability of this molecule to inhibit the growth of *C. difficile* strain 630 *in vitro* and observed an MIC of 0.5 μg/mL (Figure 5D). To establish the murine infection, C57BL/6 mice were administered intraperitoneal injections of ampicillin (200 mg/kg) every 24 h for 72 h. Mice were then given 24 h to recover and subsequently administered 5 × 10^3 spores of *C. difficile* 630 via oral gavage. Beginning 24 h after *C. difficile* gavage, mice were gavaged with antibiotics (50 mg/kg metronidazole or 15 mg/kg halicin) or vehicle (10% polyethylene glycol [PEG] 300) every 24 h for 5 days, and fecal samples were collected to quantify *C. difficile* load (Figure 5E). Excitingly, we observed that halicin resulted in *C. difficile* clearance at a greater rate than vehicle or the antibiotic metronidazole (Figure 5F), which is not only a first-line treatment for *C. difficile* infection, but also the antibiotic most similar to halicin based on Tanimoto score (Figure 2H; Table S2H). Indeed, halicin resulted in sterilization of 3 out of 4 mice after 72 h of treatment, and 4 out of 4 mice after 96 h of treatment.

Predicting New Antibiotic Candidates from Vast Chemical Libraries

After applying our deep neural network model to identify antibiotic candidates from the Drug Repurposing Hub, we subsequently explored two additional chemical libraries—the WuXi anti-tuberculosis library housed at the Broad Institute that contains 9,997 molecules, and the ZINC15 database, a virtual collection of ~1.5 billion molecules designed for *in silico* screening (Sterling and Irwin, 2015). The WuXi anti-tuberculosis library served to test our model in chemical spaces that were highly divergent from the training dataset, prior to conducting large-scale predictions in the vast ZINC15 database. We applied our empirical data gathered from the Drug Repurposing Hub molecules to re-train the original model and then applied this new model to the WuXi anti-tuberculosis library. Interestingly, we observed an upper limit prediction score of just ~0.37 for the WuXi anti-tuberculosis library (Figure S5A), which was substantially lower than the highest prediction scores observed for the Drug Repurposing Hub (upper limit ~0.97; Figure 2C). Next, we curated and empirically assayed the 200 WuXi anti-tuberculosis library compounds with the highest prediction scores and the 100 with the lowest. As expected, none of the 300 molecules that were assayed for growth inhibition against *E. coli* displayed antibacterial activity (Figures S5B and S5C; Table S5).

After again re-training our model with the empirical data gathered from these 300 WuXi anti-tuberculosis library molecules, we performed predictions on a subset of the ZINC15 database. Here, rather than screening the entire ~1.5 billion-molecule database, we focused specifically on those tranches that contained molecules with physicochemical properties that are observed in antibiotic-like compounds (Figure 6A). This more focused approach resulted in the *in silico* curation of 107,349,233 molecules; for perspective, this is two orders of magnitude larger than empirical screening permits (Brown et al., 2014), and our *in silico* screen of the library could be performed in 4 days.

After running predictions on the selected tranches of the ZINC15 database, compounds were binned based on prediction score. This resulted in 6,820 molecules with scores >0.7, 3,260 molecules with scores >0.8, and 1,070 molecules with scores >0.9 (Figure 6B; Table S6A). We compared the top 6,820 ZINC15 prediction ranks from our model (Table S6A) to numerous others, including a learned model without RDKit feature augmentation (Table S6B); a model trained exclusively on RDKit features (Table S6C); a feed-forward deep neural network model using Morgan fingerprints as the molecular representation (Table S6D); a random forest classifier using Morgan

(C) Prediction scores and Tanimoto nearest neighbor antibiotic scores of the 23 predictions that were empirically tested for growth inhibition. Yellow circles represent those molecules that displayed detectable growth inhibition of at least one pathogen. Grey circles represent inactive molecules. ZINC numbers of active molecules are shown on the right.

(D) MIC values (μg/mL) of the eight active predictions from the ZINC15 database against *E. coli* (EC), *S. aureus* (SA), *K. pneumoniae* (KP), *A. baumannii* (AB), and *P. aeruginosa* (PA). Blank regions represent no detectable growth inhibition at 128 μg/mL. Structures are shown in the same order (top to bottom) as their corresponding ZINC numbers in (C).

(E) MIC of ZINC000100032716 against *E. coli* strains harboring a range of antibiotic-resistance determinants. The *mcr-1* gene was expressed in *E. coli* BW25113. All other resistance genes were expressed in *E. coli* BW25113 Δ*bamB*Δ*tolC*. Experiments were conducted with two biological replicates. Note the minor increase in MIC in the presence of aac(6′)-Ib-cr.

(F) Same as (E) except using ZINC000225434673.

(G) Killing of *E. coli* in LB media in the presence of varying concentrations of ZINC000100032716 after 0 h (blue) and 4 h (red). The initial cell density is ~10^6 CFU/mL. Shown is the mean of two biological replicates. Bars denote absolute error.

(H) Same as (G) except using ZINC000225434673.

(I) t-SNE of all molecules from the primary training dataset (blue), the Drug Repurposing Hub (red), the WuXi anti-tuberculosis library (green), the ZINC15 molecules with prediction scores >0.9 (pink), false-positive predictions (gray), and true-positive predictions (yellow).

See also Figure S5 and Tables S5, S6, and S7.

fingerprints (Table S6E); and a support-vector machine model using Morgan fingerprints (Table S6F). Next, all molecules were rank ordered based on prediction score using our model and assessed for Tanimoto similarity to all known antibiotics. Because we were interested in identifying antibacterial molecules that were structurally dissimilar from current antibiotics, we prioritized compounds for curation with prediction scores >0.8 and Tanimoto similarities to any known antibiotic <0.4. We were able to curate 23 compounds that met these criteria for empirical testing (Figure 6C; Table S7A).

Next, we assayed these compounds for growth inhibition against *E. coli*, *S. aureus*, *Klebsiella pneumoniae*, *A. baumannii*, and *P. aeruginosa*. Indeed, even though our model was trained on growth inhibition against *E. coli*, because the majority of antibiotics display activity against numerous bacterial species, we reasoned that it could be possible that some of these predictions had bioactivity against diverse pathogens. Excitingly, we observed that 8 of the 23 molecules displayed detectable growth inhibitory activity against at least one of the tested species (Figures 6C, 6D, and S5D–S5K; Tables S7A and S7B).

Of note, we observed two compounds that displayed potent broad-spectrum activity, ZINC000100032716 and ZINC000225434673 (Figure 6D), and overcame an array of common resistance determinants (Figures 6E and 6F). Interestingly, ZINC000100032716 has structural features found in both quinolones and sulfa drugs, yet remains highly divergent from known antibiotics (enrofloxacin nearest neighbor with Tanimoto similarity ~0.39) and was only weakly impacted by plasmid-borne fluoroquinolone resistance via aac(6′)-Ib-cr (Figure 6E) or chromosomal resistance via mutation of *gyrA* (Figures S5L and S5M). Moreover, both ZINC000100032716 and ZINC000225434673 displayed bactericidal activity against *E. coli* in rich medium (Figures 6G and 6H), with the latter resulting in complete sterilization after just 4 h of treatment. Given its novel structure (nitromide nearest neighbor with Tanimoto similarity ~0.16) and low predicted toxicity in humans (Table S7A), we posit that ZINC000225434673 warrants further investigation.

Last, upon determining the antibacterial properties of these 23 predicted molecules, we ventured to understand their chemical relationships to the training data. We therefore analyzed the structural relationships between these compounds, ZINC15 molecules with prediction scores >0.9, our primary training set, the Drug Repurposing Hub, and the WuXi anti-tuberculosis library (Figure 6I). Intriguingly, our analysis revealed that the WuXi anti-tuberculosis library contained molecules that largely occupied a distinct chemical space relative to compounds with antibacterial activity, consistent with our results showing that even the highest predicted of these were unable to inhibit the growth of *E. coli*. Moreover, this analysis emphasized the fact that the predicted compounds resided in varied chemical spaces, suggesting that our model was largely unbiased in enriching for specific chemical moieties—at least below our Tanimoto nearest neighbor threshold of 0.4.

DISCUSSION

The prevalence of antibiotic resistance is rapidly increasing on a global scale. Concurrently, the steadily declining productivity in clinically implementing new antibiotics due to the high risk of early discovery and low return on investment is exacerbating this problem (Brown and Wright, 2016). Therefore, the development of new approaches that can substantially decrease the cost and increase the rate of antibiotic discovery is essential to reinfuse the pipeline with a steady stream of candidates that show promise as next-generation therapeutics. The adoption of machine learning approaches is ideally suited to address these hurdles. Indeed, modern neural molecular representations have the potential to: (1) decrease the cost of lead molecule identification because screening is limited to gathering appropriate training data, (2) increase the true positive rate of identifying structurally novel compounds with the desired bioactivity, and (3) decrease the time and labor required to find these ideal compounds from months or years to weeks.

In this study, we applied neural molecular representations to predict antibacterial compounds *in silico* from a collection of >107 million compounds. We first trained a deep neural network model with empirical data analyzing *E. coli* growth inhibition by molecules from a widely available FDA-approved drug library supplemented with a modest natural product library, totaling 2,335 molecules. Next, we applied the resulting model to predict antibacterial compounds from the Drug Repurposing Hub. Excitingly, among the most highly predicted molecules, our model performed well (51.5% accuracy) and ultimately resulted in identifying halicin as a broad-spectrum bactericidal antibiotic with exceptional *in vivo* efficacy. The low structural similarity of halicin to its nearest neighbor antibiotic, metronidazole (Tanimoto similarity ~0.21), showed that our approach was capable of generalization, thus permitting access to new antibiotic chemistry.

We subsequently expanded our prediction space to include the WuXi anti-tuberculosis library, as well as a subset of the ZINC15 database comprising 107,349,233 molecules, in order to identify additional candidate antibacterial molecules. We did not observe growth inhibition from any molecules empirically tested from the WuXi library, in agreement with the correspondingly low model prediction scores (upper limit ~0.37). However, from among the 23 molecules from the ZINC15 database that we curated for empirical testing, we observed that eight of these validated as true positives in at least one of the tested pathogens. Importantly, these compounds were curated based on high prediction scores and low Tanimoto similarities to known antibiotics, providing further support that our model was able to generalize to new chemistries. Remarkably, two of these eight molecules, ZINC000100032716 and ZINC000225434673, displayed broad-spectrum activity and maintained activity against *E. coli* harboring an array of resistance determinants.

It is important to emphasize that machine learning is imperfect. Therefore, the success of deep neural network model-guided antibiotic discovery rests heavily on the coupling of these approaches to appropriate experimental designs. The first consideration should be the assay design for training: what is the biological outcome that is desired after cells are exposed to compounds? In the proof-of-concept described herein, we selected growth inhibition as the biological

property on which we would gather training data, since this generally results in a reasonable proportion of active compounds relative to the size of the screening library, and quite easily generates reproducible data. However, the number of bacterial phenotypes that could theoretically result in efficacious antibiotics is expansive (Farha and Brown, 2015; Kohanski et al., 2010), and so long as it is possible to gather a sufficient quantity of reproducible hit compounds from a primary screen, deep neural network approaches would be well-suited to predict additional molecules with the desired biological property. Indeed, where our screen was largely mechanism of action agnostic, future applications could incorporate phenotypic screening conditions that enrich for molecules against specific biological targets (Stokes and Brown, 2015; Stokes et al., 2016, 2017; Yang et al., 2019a).

The second consideration is the composition of the training data itself: on what chemistry should the model be trained? It is important to use training data that have sufficient chemical diversity in both active and inactive compounds, as well as appropriate pharmacology/absorption, distribution, metabolism, and excretion [ADME]/toxicity properties for *in vivo* application. If all active molecules are structurally similar, the model will be unable to generalize to new scaffolds. Moreover, model accuracy deteriorates as the training set and prediction set diverge. As such, there exists a tension of sorts between prediction accuracy and chemical generalization, and it is advantageous to have the broadest structural variation possible in the training phase to maximize the probability of successful generalization in new chemical spaces. In our case, the desire to train on a supplemented FDA-approved drug library was to offer the capability of performing a small screen and simultaneously capturing substantial chemical diversity with desired pharmacology/ADME/toxicity properties. While mining pre-existing screening datasets could have been implemented, we reasoned that at this early stage in the application of machine learning for antibiotic discovery, a carefully controlled training set would allow for more tractable predictions that avoided potentially unfavorable molecules. Nevertheless, given the increasing volume of screening data that exists (Wang et al., 2017), carefully leveraging these resources could result in millions of molecular graph-biological property relationships, provided that the data are of adequate quality and methodological uniformity so that erroneous predictions could be minimized.

The third consideration is in prediction prioritization: what is the most appropriate approach to selecting tens of molecules for follow-up investigation from thousands of strongly predicted compounds? Because we aimed to identify new antibacterial candidates, our prioritization scheme involved the selection of molecules that were (1) given a high prediction score, (2) structurally unique relative to clinical antibiotics based on Tanimoto nearest neighbor analyses, and in some cases, (3) unlikely to display toxicity. Indeed, this approach allowed us to identify halicin, as well as numerous attractive compounds from the ZINC15 database. It should be noted here, however, that investigators can encounter limitations in acquiring predicted compounds in quantities sufficient to perform experiments. This can be due to the inability to synthesize predicted molecules, prohibitive costs of synthesizing those that can, and/or compound instability in aqueous solution. However, emerging models in retrosynthesis and physicochemical property prediction may overcome these limitations in the near future (Coley et al., 2018; Gao et al., 2018).

Where our deep neural network model was trained using a targeted dataset, future endeavors could aim to assemble chemical libraries designed for model training on a task-by-task basis, which may contain on the order of perhaps $\sim 10^5$ compounds of diverse structure. In the context of antibacterial discovery, these training libraries should contain molecules with physicochemical properties consistent with antibacterial drugs (Tommasi et al., 2015), yet sufficiently diverse such that the model can generalize to unconventional chemistry. Furthermore, with repeated training cycles across phylogenetically diverse species, it may be possible to predict molecules with antibacterial activity against a specified spectrum of pathogens. This has the promise to result in narrow-spectrum agents that can be administered systemically without damaging the host microbiota. Moreover, by training on multidrug-resistant pathogens, it may be possible to identify scaffolds that overcome pre-existing resistance determinants. Overall, our results suggest that the time is ripe for the application of modern machine learning approaches for antibiotic discovery—such efforts could increase the rate at which new molecular entities are discovered, decrease the resources required to identify these molecules, and decrease associated costs. Deep learning approaches could therefore enable us to expand our antibiotic arsenal and help outpace the dissemination of resistance.

STAR★METHODS

Detailed methods are provided in the online version of this paper and include the following:

- KEY RESOURCES TABLE
- LEAD CONTACT AND MATERIALS AVAILABILITY
- METHODS DETAILS
  - Model training and predictions
  - Additional molecule-level features
  - Hyperparameter optimization
  - Ensembling
  - Chemical analyses
  - Chemical screening
  - Growth inhibition assays
  - Bacterial cell killing assays
  - Mutant generation
  - RNA sequencing
  - $DiSC_3(5)$ assays
- EXPERIMENTAL MODEL AND SUBJECT DETAILS
  - baumannii mouse infection model
  - C. difficile mouse infection model
- DATA AND CODE AVAILABILITY
  - Code availability
  - RNA sequencing data
- ADDITIONAL RESOURCES
  - Online model availability

SUPPLEMENTAL INFORMATION

Supplemental Information can be found online at https://doi.org/10.1016/j.cell.2020.01.021.

ACKNOWLEDGMENTS

We thank Caleb Bashor from Rice University for valuable discussions, Gerry Wright from McMaster University for antibiotic-resistant strains of *E. coli*, and Michael Gilmore from Harvard Medical School for *S. aureus* RN4220 and Δ*dsp1*. This work was supported by the Abdul Latif Jameel Clinic for Machine Learning in Health; the Defence Threat Reduction Agency (HDTRA1-15-1-0051 to J.J.C.); the Broad Institute of MIT and Harvard (to J.J.C.); the DARPA Make-It program under contract Army Research Office (W911NF-16-2-0023 to T.S.J. and R.B.); the Defence Threat Reduction Agency (HR00111920025 to T.S.J. and R.B.); the Canadian Institutes of Health Research (FRN 143215 to E.D.B.); the Canadian Foundation for Innovation (to E.D.B.); the Canada Research Chairs Program (Tier 1 to E.D.B.); the Banting Fellowships Program (393360 to J.M.S.); the Canadian Institutes of Health Research (scholarship to C.R.M.); the Human Frontier Science Program (LT000975/2016-L to Z.B.-A.); the Broad Institute Tuberculosis Donor Group and the Pershing Square Foundation (to Z.B.-A. and V.M.T.); the Swiss National Science Foundation (P2ELP2_181884 to A.C.-P.); the Broad Institute of MIT and Harvard (to A.H.B.); NIH Early Investigator Award (DP5-OD-024590 to A.H.B.); the National Science Foundation Graduate Research Fellowship Program (1122374 to I.W.A.); and by a generous gift from Anita and Josh Bekenstein.

AUTHOR CONTRIBUTIONS

Conceptualization, J.M.S., T.S.J., R.B., and J.J.C.; Model Development and Training, J.M.S., K.Y., K.S., W.J., and I.W.A.; Mechanistic Investigations, J.M.S., S.F., Z.B.-A., V.M.T., A.C.-P., and A.H.B.; Mouse Models, A.C.-R., N.M.D., C.R.M., and L.A.C.; Data Representation, J.M.S. and E.J.C.; Manuscript – Writing & Editing, J.M.S., K.Y., K.S., I.W.A., R.B., and J.J.C.; Funding Acquisition, J.M.S., A.H.B., E.D.B., T.S.J., R.B., and J.J.C.; Supervision, G.M.C., E.D.B., T.S.J., R.B., and J.J.C.

DECLARATION OF INTERESTS

J.J.C. is scientific co-founder and SAB chair of EnBiotix, an antibiotic drug discovery company.

Received: August 27, 2019
Revised: December 4, 2019
Accepted: January 15, 2020
Published: February 20, 2020

REFERENCES

Abeel, T., Van Parys, T., Saeys, Y., Galagan, J., and Van de Peer, Y. (2012). GenomeView: a next-generation genome browser. Nucleic Acids Res. *40*, e12.

Angus, B.L., Carey, A.M., Caron, D.A., Kropinski, A.M., and Hancock, R.E. (1982). Outer membrane permeability in *Pseudomonas aeruginosa*: comparison of a wild-type with an antibiotic-supersusceptible mutant. Antimicrob. Agents Chemother. *21*, 299–309.

Balaban, N.Q., Helaine, S., Lewis, K., Ackermann, M., Aldridge, B., Andersson, D.I., Brynildsen, M.P., Bumann, D., Camilli, A., Collins, J.J., et al. (2019). Definitions and guidelines for research on antibiotic persistence. Nat. Rev. Microbiol. *17*, 441–448.

Brown, E.D., and Wright, G.D. (2016). Antibacterial drug discovery in the resistance era. Nature *529*, 336–343.

Brown, D.G., May-Dracka, T.L., Gagnon, M.M., and Tommasi, R. (2014). Trends and exceptions of physical properties on antibacterial activity for Gram-positive and Gram-negative pathogens. J. Med. Chem. *57*, 10144–10161.

Camacho, D.M., Collins, K.M., Powers, R.K., Costello, J.C., and Collins, J.J. (2018). Next-generation machine learning for biological networks. Cell *173*, 1581–1592.

Clardy, J., Fischbach, M.A., and Walsh, C.T. (2006). New antibiotics from bacterial natural products. Nat. Biotechnol. *24*, 1541–1550.

Coates, A.R., and Hu, Y. (2008). Targeting non-multiplying organisms as a way to develop novel antimicrobials. Trends Pharmacol. Sci. *29*, 143–150.

Coley, C.W., Jin, W., Rogers, L., Jamison, T.F., Jaakkola, T.S., Green, W.H., Barzilay, R., and Jensen, K.F. (2018). A graph-convolutional neural network model for the prediction of chemical reactivity. Chem. Sci. (Camb.) *10*, 370–377.

Corsello, S.M., Bittker, J.A., Liu, Z., Gould, J., McCarren, P., Hirschman, J.E., Johnston, S.E., Vrcic, A., Wong, B., Khan, M., et al. (2017). The Drug Repurposing Hub: a next-generation drug library and information resource. Nat. Med. *23*, 405–408.

Cox, G., Sieron, A., King, A.M., De Pascale, G., Pawlowski, A.C., Koteva, K., and Wright, G.D. (2017). A common platform for antibiotic dereplication and adjuvant discovery. Cell Chem. Biol. *24*, 98–109.

D'haeseleer, P. (2005). How does gene expression clustering work? Nat. Biotechnol. *23*, 1499–1501.

Datsenko, K.A., and Wanner, B.L. (2000). One-step inactivation of chromosomal genes in *Escherichia coli* K-12 using PCR products. Proc. Natl. Acad. Sci. USA *97*, 6640–6645.

De, S.K., Stebbins, J.L., Chen, L.H., Riel-Mehan, M., Machleidt, T., Dahl, R., Yuan, H., Emdadi, A., Barile, E., Chen, V., et al. (2009). Design, synthesis, and structure-activity relationship of substrate competitive, selective, and in vivo active triazole and thiadiazole inhibitors of the c-Jun N-terminal kinase. J. Med. Chem. *52*, 1943–1952.

Dietterich, T.G. (2000). Ensemble Methods in Machine Learning: Multiple Classifier Systems (Springer).

Edwards, A.N., and McBride, S.M. (2016). Isolating and purifying *Clostridium difficile* spores. Methods Mol. Biol. *1476*, 117–128.

Farha, M.A., and Brown, E.D. (2015). Unconventional screening approaches for antibiotic discovery. Ann. N Y Acad. Sci. *1354*, 54–66.

Farha, M.A., Verschoor, C.P., Bowdish, D., and Brown, E.D. (2013). Collapsing the proton motive force to identify synergistic combinations against *Staphylococcus aureus*. Chem. Biol. *20*, 1168–1178.

Farha, M.A., French, S., Stokes, J.M., and Brown, E.D. (2018). Bicarbonate alters bacterial susceptibility to antibiotics by targeting the proton motive force. ACS Infect. Dis. *4*, 382–390.

Gao, H., Struble, T.J., Coley, C.W., Wang, Y., Green, W.H., and Jensen, K.F. (2018). Using machine learning to predict suitable conditions for organic reactions. ACS Cent. Sci. *4*, 1465–1476.

Gayvert, K.M., Madhukar, N.S., and Elemento, O. (2016). A data-driven approach to predicting successes and failures of clinical trials. Cell Chem. Biol. *23*, 1294–1301.

Gough, E., Shaikh, H., and Manges, A.R. (2011). Systematic review of intestinal microbiota transplantation (fecal bacteriotherapy) for recurrent *Clostridium difficile* infection. Clin. Infect. Dis. *53*, 994–1002.

Hurdle, J.G., O'Neill, A.J., Chopra, I., and Lee, R.E. (2011). Targeting bacterial membrane function: an underexploited mechanism for treating persistent infections. Nat. Rev. Microbiol. *9*, 62–75.

Jang, S., Yu, L.R., Abdelmegeed, M.A., Gao, Y., Banerjee, A., and Song, B.J. (2015). Critical role of c-jun N-terminal protein kinase in promoting mitochondrial dysfunction and acute liver injury. Redox Biol. *6*, 552–564.

Jaskowiak, P.A., Campello, R.J., and Costa, I.G. (2014). On the selection of appropriate distances for gene expression data clustering. BMC Bioinformatics *15* (*Suppl 2*), S2.

Karp, P.D. (2001). Pathway databases: a case study in computational symbolic theories. Science *293*, 2040–2044.

Karp, P.D., Latendresse, M., Paley, S.M., Krummenacker, M., Ong, Q.D., Billington, R., Kothari, A., Weaver, D., Lee, T., Subhraveti, P., et al. (2016). Pathway Tools version 19.0 update: software for pathway/genome informatics and systems biology. Brief. Bioinform. *17*, 877–890.

Keseler, I.M., Mackie, A., Peralta-Gil, M., Santos-Zavaleta, A., Gama-Castro, S., Bonavides-Martínez, C., Fulcher, C., Huerta, A.M., Kothari, A., Krummenacker, M., et al. (2013). EcoCyc: fusing model organism databases with systems biology. Nucleic Acids Res. *41*, D605–D612.

Kohanski, M.A., Dwyer, D.J., and Collins, J.J. (2010). How antibiotics kill bacteria: from targets to networks. Nat. Rev. Microbiol. *8*, 423–435.

Landrum, G. (2006). RDKit: Open-source cheminformatics. https://rdkit.org/docs/index.html.

Lee, C.R., Lee, J.H., Park, M., Park, K.S., Bae, I.K., Kim, Y.B., Cha, C.J., Jeong, B.C., and Lee, S.H. (2017). Biology of *Acinetobacter baumannii*: pathogenesis, antibiotic resistance mechanisms, and prospective treatment options. Front. Cell. Infect. Microbiol. *7*, 55.

Li, H., and Durbin, R. (2009). Fast and accurate short read alignment with Burrows-Wheeler transform. Bioinformatics *25*, 1754–1760.

Lobritz, M.A., Belenky, P., Porter, C.B., Gutierrez, A., Yang, J.H., Schwarz, E.G., Dwyer, D.J., Khalil, A.S., and Collins, J.J. (2015). Antibiotic efficacy is linked to bacterial cellular respiration. Proc. Natl. Acad. Sci. USA *112*, 8173–8180.

Loewenstein, Y., Portugaly, E., Fromer, M., and Linial, M. (2008). Efficient algorithms for accurate hierarchical clustering of huge datasets: tackling the entire protein space. Bioinformatics *24*, i41–i49.

Love, M.I., Huber, W., and Anders, S. (2014). Moderated estimation of fold change and dispersion for RNA-seq data with DESeq2. Genome Biol. *15*, 550.

Manson, M.D., Tedesco, P., Berg, H.C., Harold, F.M., and Van der Drift, C. (1977). A protonmotive force drives bacterial flagella. Proc. Natl. Acad. Sci. USA *74*, 3060–3064.

Mauri, A., Consonni, V., Pavan, M., and Todeschini, R. (2006). Dragon software: an easy approach to molecular descriptor calculations. MATCH Commun. Math. Comput. Chem. *56*, 237–248.

Mayr, A., Klambauer, G., Unterthiner, T., Steijaert, M., Wegner, J.K., Ceulemans, H., Clevert, D.A., and Hochreiter, S. (2018). Large-scale comparison of machine learning methods for drug target prediction on ChEMBL. Chem. Sci. (Camb.) *9*, 5441–5451.

Moriwaki, H., Tian, Y.S., Kawashita, N., and Takagi, T. (2018). Mordred: a molecular descriptor calculator. J. Cheminform. *10*, 4.

O'Neill, J. (2014). Antimicrobial Resistance: Tackling a Crisis for the Health and Wealth of Nations (Review on Antimicrobial Resistance, 2014).

Ortholand, J.Y., and Ganesan, A. (2004). Natural products and combinatorial chemistry: back to the future. Curr. Opin. Chem. Biol. *8*, 271–280.

Paul, K., Erhardt, M., Hirano, T., Blair, D.F., and Hughes, K.T. (2008). Energy source of flagellar type III secretion. Nature *451*, 489–492.

Perez, F., Hujer, A.M., Hujer, K.M., Decker, B.K., Rather, P.N., and Bonomo, R.A. (2007). Global challenge of multidrug-resistant *Acinetobacter baumannii*. Antimicrob. Agents Chemother. *51*, 3471–3484.

P.E.W. Trusts (2019). Five-year analysis shows continued deficiencies in antibiotic development. https://www.pewtrusts.org/en/research-and-analysis/data-visualizations/2019/five-year-analysis-shows-continued-deficiencies-in-antibiotic-development.

Robinson, M.D., McCarthy, D.J., and Smyth, G.K. (2010). edgeR: a Bioconductor package for differential expression analysis of digital gene expression data. Bioinformatics *26*, 139–140.

Rogers, D., and Hahn, M. (2010). Extended-connectivity fingerprints. J. Chem. Inf. Model. *50*, 742–754.

Sandegren, L., Lindqvist, A., Kahlmeter, G., and Andersson, D.I. (2008). Nitrofurantoin resistance mechanism and fitness cost in *Escherichia coli*. J. Antimicrob. Chemother. *62*, 495–503.

Shioi, J.I., Galloway, R.J., Niwano, M., Chinnock, R.E., and Taylor, B.L. (1982). Requirement of ATP in bacterial chemotaxis. J. Biol. Chem. *257*, 7969–7975.

Shishkin, A.A., Giannoukos, G., Kucukural, A., Ciulla, D., Busby, M., Surka, C., Chen, J., Bhattacharyya, R.P., Rudy, R.F., Patel, M.M., et al. (2015). Simultaneous generation of many RNA-seq libraries in a single reaction. Nat. Methods *12*, 323–325.

Sterling, T., and Irwin, J.J. (2015). ZINC 15–ligand discovery for everyone. J. Chem. Inf. Model. *55*, 2324–2337.

Stokes, J.M., and Brown, E.D. (2015). Chemical modulators of ribosome biogenesis as biological probes. Nat. Chem. Biol. *11*, 924–932.

Stokes, J.M., French, S., Ovchinnikova, O.G., Bouwman, C., Whitfield, C., and Brown, E.D. (2016). Cold stress makes *Escherichia coli* susceptible to glycopeptide antibiotics by altering outer membrane integrity. Cell Chem. Biol. *23*, 267–277.

Stokes, J.M., MacNair, C.R., Ilyas, B., French, S., Côté, J.P., Bouwman, C., Farha, M.A., Sieron, A.O., Whitfield, C., Coombes, B.K., and Brown, E.D. (2017). Pentamidine sensitizes Gram-negative pathogens to antibiotics and overcomes acquired colistin resistance. Nat. Microbiol. *2*, 17028.

Stokes, J.M., Gutierrez, A., Lopatkin, A.J., Andrews, I.W., French, S., Matic, I., Brown, E.D., and Collins, J.J. (2019a). A multiplexable assay for screening antibiotic lethality against drug-tolerant bacteria. Nat. Methods *16*, 303–306.

Stokes, J.M., Lopatkin, A.J., Lobritz, M.A., and Collins, J.J. (2019b). Bacterial Metabolism and Antibiotic Efficacy. Cell Metab. *30*, 251–259.

Surawicz, C.M., Brandt, L.J., Binion, D.G., Ananthakrishnan, A.N., Curry, S.R., Gilligan, P.H., McFarland, L.V., Mellow, M., and Zuckerbraun, B.S. (2013). Guidelines for diagnosis, treatment, and prevention of *Clostridium difficile* infections. Am. J. Gastroenterol. *108*, 478–498, quiz 499.

Taber, H.W., Mueller, J.P., Miller, P.F., and Arrow, A.S. (1987). Bacterial uptake of aminoglycoside antibiotics. Microbiol. Rev. *51*, 439–457.

Tally, F.P., Goldin, B.R., Sullivan, N., Johnston, J., and Gorbach, S.L. (1978). Antimicrobial activity of metronidazole in anaerobic bacteria. Antimicrob. Agents Chemother. *13*, 460–465.

Tommasi, R., Brown, D.G., Walkup, G.K., Manchester, J.I., and Miller, A.A. (2015). ESKAPEing the labyrinth of antibacterial discovery. Nat. Rev. Drug Discov. *14*, 529–542.

Wang, Y., Bryant, S.H., Cheng, T., Wang, J., Gindulyte, A., Shoemaker, B.A., Thiessen, P.A., He, S., and Zhang, J. (2017). PubChem BioAssay: 2017 update. Nucleic Acids Res. *45* (D1), D955–D963.

Winston, J.A., Thanissery, R., Montgomery, S.A., and Theriot, C.M. (2016). Cefoperazone-treated mouse model of clinically-relevant *Clostridium difficile* strain R20291. J. Vis. Exp. (118), 54850.

Wright, G.D. (2017). Opportunities for natural products in 21st century antibiotic discovery. Nat. Prod. Rep. *34*, 694–701.

Wu, M., Maier, E., Benz, R., and Hancock, R.E. (1999). Mechanism of interaction of different classes of cationic antimicrobial peptides with planar bilayers and with the cytoplasmic membrane of *Escherichia coli*. Biochemistry *38*, 7235–7242.

Wu, Z., Ramsundar, B., Feinberg, E.N., Gomes, J., Geniesse, C., Pappu, A.S., Leswing, K., and Pande, V. (2017). MoleculeNet: a benchmark for molecular machine learning. Chem. Sci. (Camb.) *9*, 513–530.

Yamaguchi, A., Ohmori, H., Kaneko-Ohdera, M., Nomura, T., and Sawai, T. (1991). Delta pH-dependent accumulation of tetracycline in *Escherichia coli*. Antimicrob. Agents Chemother. *35*, 53–56.

Yang, J.H., Wright, S.N., Hamblin, M., McCloskey, D., Alcantar, M.A., Schrübbers, L., Lopatkin, A.J., Satish, S., Nili, A., Palsson, B.O., et al. (2019a). A white-box machine learning approach for revealing antibiotic mechanisms of action. Cell *177*, 1649–1661.

Yang, K., Swanson, K., Jin, W., Coley, C., Eiden, P., Gao, H., Guzman-Perez, A., Hopper, T., Kelley, B., Mathea, M., et al. (2019b). Analyzing learned molecular representations for property prediction. J. Chem. Inf. Model. *59*, 3370–3388.

Yoshimura, F., and Nikaido, H. (1982). Permeability of *Pseudomonas aeruginosa* outer membrane to hydrophilic solutes. J. Bacteriol. *152*, 636–642.

Zampieri, M., Zimmermann, M., Claassen, M., and Sauer, U. (2017). Nontargeted metabolomics reveals the multilevel response to antibiotic perturbations. Cell Rep. *19*, 1214–1228.

Zhu, Y.Y., Machleder, E.M., Chenchik, A., Li, R., and Siebert, P.D. (2001). Reverse transcriptase template switching: a SMART approach for full-length cDNA library construction. Biotechniques *30*, 892–897.

STAR★METHODS

KEY RESOURCES TABLE

REAGENT or RESOURCE	SOURCE	IDENTIFIER
Bacterial and Virus Strains		
Escherichia coli BW25113	CGSC	7636
Staphylococcus aureus USA 300	ATCC	TCH1516
Klebsiella pneumoniae ATCC 700721	ATCC	700721
Acinetobacter baumannii ATCC 17978	ATCC	17978
Pseudomonas aeruginosa PA01	ATCC	47085
Clostridioides difficile 630	ATCC	BAA-1382
Mycobacterium tuberculosis H37Rv	ATCC	25618
Antibiotic-resistant isolates from CDC	CDC AR Isolate Bank	See Table S3 for unique identifiers
Chemicals, Peptides, and Recombinant Proteins		
SU3327 (halicin)	TCI chemicals	A2940
ZINC000013517522	Vitas-M	STL439768
ZINC000006719085	Vitas-M	STK708267
ZINC000101675810	Vitas-M	STK940888
ZINC000101676256	Vitas-M	STK929481
ZINC000018090096	Specs	AP-216/15652011
ZINC000169457956	Specs	AP-216/15652003
ZINC000004481415	IBScreen	STOCK1S-22001
ZINC000019771150	ChemBridge	5773027
ZINC000001387673	ChemBridge	5253687
ZINC000005510605	TimTec	ST50999405
ZINC000022865640	TimTec	ST50990898
ZINC000015134557	TimTec	ST4019615
ZINC000098210492	KeyOrganics	AS-8081
ZINC000100506795	TimTec	ST50222762
ZINC000238901709	TimTec	ST100643
ZINC000004623615	TimTec	ST4104620
ZINC000100032716	TimTec	ST45053787
ZINC000584578353	PI Chemicals	PI-31452
ZINC000006661600	Ambeed	A107950
ZINC000225434673	Ambinter	Amb22349288
ZINC000006599408	Ambinter	Amb17836664
ZINC000038586996	Ambinter	Amb19958926
ZINC000001735150	NCI Plated 2007	200689
Deposited Data		
RNA sequencing datasets	This study	BioProject ID: PRJNA598708
Experimental Models: Organisms/Strains		
Mouse: BALB/c	Charles River	028
Mouse: C57BL/6	Charles River	C57BL/6NCrl
Oligonucleotides		
TAGCCGGGCAGATGCCCGGCAAGAGAGAA TTACACTTCGGTTAAGGTGATATTCCGGG GATCCGTCGACC	This study	AB5044
ACCTTGTAATCTGCTGGCACGCAAAAT TACTTTCACATGGAGTCTTTATGT GTAGGCTGGAGCTGCTTCG	This study	AB5045

(*Continued on next page*)

Continued

REAGENT or RESOURCE	SOURCE	IDENTIFIER
tgcaaaataatatgcaccacgacggcggtcagaaaaataa	This study	AB5046
gaagcgttacttcgcgatctgatcaacgattcgtggaatc	This study	AB5047
Software and Algorithms		
Chemprop	Yang et al., 2019b	https://github.com/swansonk14/chemprop
RDKit	Landrum, 2006	https://github.com/rdkit
BWA	Li and Durbin, 2009	https://github.com/lh3/bwa
DESeq2	Love et al., 2014	https://bioconductor.org/packages/release/bioc/html/DESeq2.html
edgeR	Robinson et al., 2010	https://bioconductor.org/packages/release/bioc/html/edgeR.html
GenomeView	Abeel et al., 2012	https://genomeview.org
EcoCyc Pathway Tools	Keseler et al., 2013	https://ecocyc.org

LEAD CONTACT AND MATERIALS AVAILABILITY

Further information and requests for resources and reagents should be directed to James J. Collins (jimjc@mit.edu). All unique/stable reagents generated in this study are available from the Lead Contact with a completed Materials Transfer Agreement.

METHODS DETAILS

Model training and predictions

A directed-message passing neural network (Chemprop), like other message passing neural networks, learns to predict molecular properties directly from the graph structure of the molecule, where atoms are represented as nodes and bonds are represented as edges. For every molecule, we reconstructed the molecular graph corresponding to each compound's SMILES string and determined the set of atoms and bonds using the open-source package RDKit (Landrum, 2006). Next, we initialized a feature vector, as described in Yang et al. (2019b), for each atom and bond based on computable features:

1. **Atom features**: atomic number, number of bonds for each atom, formal charge, chirality, number of bonded hydrogens, hybridization, aromaticity, atomic mass.
2. **Bond features**: bond type (single/double/triple/aromatic), conjugation, ring membership, stereochemistry.

The model applies a series of message passing steps where it aggregates information from neighboring atoms and bonds to build an understanding of local chemistry. In Chemprop, on each step of message passing, each bond's featurization is updated by summing the featurization of neighboring bonds, concatenating the current bond's featurization with the sum, and then applying a single neural network layer with non-linear activation. After a fixed number of message-passing steps, the learned featurizations across the molecule are summed to produce a single featurization for the whole molecule. Finally, this featurization is fed through a feed-forward neural network that outputs a prediction of the property of interest. Since the property of interest in our application was the binary classification of whether a molecule inhibits the growth of *E. coli*, the model is trained to output a number between 0 and 1, which represents its prediction about whether the input molecule is growth inhibitory.

In addition to the basic D-MPNN architecture described above, we employed three model optimizations (Yang et al., 2019b):

Additional molecule-level features

While the message passing paradigm is excellent for extracting features that depend on local chemistry, it can struggle to extract global molecular features. This is especially true for large molecules, where the longest path through the molecule may be longer than the number of message-passing iterations performed, meaning information from one side of the molecule does not inform the features on the other side of the molecule. For this reason, we chose to concatenate the molecular representation that is learned via message passing with 200 additional molecule-level features computed with RDKit.

Hyperparameter optimization

The performance of machine learning models is known to depend critically on the choice of hyperparameters, such as the size of the neural network layers, which control how and what the model is able to learn. We used the Bayesian hyperparameter optimization scheme, with 20 iterations of optimization to improve the hyperparameters of our model (see table below). Baysian hyperparameter

optimization learns to select optimal hyperparameters based on performance using prior hyperparameter settings, allowing for rapid identification of the best set of hyperparameters for any model.

Hyperparameter	Range	Value
Number of message-passing steps	[2, 6]	5
Neural network hidden size	[300, 2400]	1600
Number of feed-forward layers	[1, 3]	1
Dropout probability	[0, 0.4]	0.35

Ensembling

Another standard machine learning technique used to improve performance is ensembling, where several copies of the same model architecture with different random initial weights are trained and their predictions are averaged. We used an ensemble of 20 models, with each model trained on a different random split of the data (Dietterich, 2000).

Our initial training dataset consisted of 2,335 molecules, with 120 compounds (5.14%) showing growth inhibitory activity against *E. coli*, as defined by endpoint $OD_{600} < 0.2$. We performed predictions on the Drug Repurposing Hub, consisting of 6,111 unique molecules; the WuXi anti-tuberculosis library, consisting of 9,997 unique molecules; and tranches of the ZINC15 database. The ZINC15 tranches that we used for molecular predictions were selected based on their likelihood to contain antibiotic-like molecules; these tranches included: 'AA', 'AB', 'BA', 'BB', 'CA', 'CB', 'CD', 'DA', 'DB', 'EA', 'EB', 'FA', 'FB', 'GA', 'GB', 'HA', 'HB', 'IA', 'IB', 'JA', 'JB', 'JC', 'JD', 'KA', 'KB', 'KC', 'KD', 'KE', 'KF', 'KG', 'KH', 'KI', 'KJ', and 'KK', constituting a dataset of 107,349,233 unique molecules.

Our experimental procedure consisted of four phases: (1a) a training phase to evaluate the optimized but non-ensembled model and (1b) training the ensemble of optimized models; (2) a prediction phase; (3) a retraining phase; and (4) a final prediction phase. We began by evaluating our model on the training set of 2,335 molecules using all optimizations except for ensembling, in order to determine the best performance of a single model. Here, we randomly split the dataset into 80% training data, 10% validation data, and 10% test data. We trained our model on the training data for 30 epochs, where an epoch is defined as a single pass through all of the training data, and we evaluated it on the validation data at the end of each epoch. After training was complete, we used the model parameters that performed best on the validation data and tested the model with those parameters on the test data. We repeated this procedure with 20 different random splits of the data and averaged the results. After we were satisfied with model performance, we conducted predictions on new datasets. Since we wanted to maximize the amount of training data and were no longer interested in measuring performance on the test set, we trained new models on the training data from each of 20 random splits, each with 90% training data, 10% validation data, and no test data.

The ensemble consisting of 20 models is the model that was applied first to the Drug Repurposing Hub, and then the WuXi anti-tuberculosis library. After empirically testing the highest and lowest predicted molecules from these libraries for growth inhibition against *E. coli*, we included all these data into our original training sets to create a new training set. The updated training set contained 2,911 unique molecules, with 232 (7.97%) showing growth inhibitory activity. We next used our retrained model to make predictions on the aforementioned subset of the ZINC15 database. We selected all molecules with a prediction score > 0.7, which resulted in 6,820 compounds. All molecules selected for curation were subsequently cross-referenced with SciFinder to ensure that these were not clinical antibiotics.

We lastly compared the prediction outputs of our augmented D-MPNN with a D-MPNN without RDKit features; a feedforward DNN model with the same depth as our D-MPNN model with hyperparameter optimization using RDKit features only; the same DNN instead using Morgan fingerprints (radius 2) as the molecular representation; and RF and SVM models using the same Morgan fingerprint representations. We used the scikit-learn implementation of a random forest classifier with all of the default parameters except for the number of trees, where we used 500 instead of 10. When making predictions, we output the growth inhibition probability for each molecule according to the random forest, which is the proportion of trees in the model that predict a 1 for that molecule. Similarly, we used the scikit-learn implementation of a support vector machine with all of the default parameters. When making predictions, we output the signed distance between the Morgan fingerprint of the molecule and the separating hyperplane that is learned by the SVM. This number represents how much the model predicts a molecule is antibacterial, with large positive distances meaning most likely antibacterial and large negative distances meaning most likely not. Although the signed distance is not a probability, it can still be used to rank the molecules according to how likely they are to be antibacterial.

To predict the toxicity of molecules for possible *in vivo* applications, we trained a Chemprop model on the ClinTox dataset. This dataset consisted of 1,478 molecules, each with two binary properties: (a) clinical trial toxicity and (b) FDA-approval status. Of these 1,478 molecules, 94 (6.36%) had clinical toxicity and 1,366 (92.42%) were FDA approved. Using the same methodology as described in phase (1) of our experimental procedure, the Chemprop model was trained on both properties simultaneously and learned a single molecular representation that was used by the feed-forward neural network layers to predict toxicity. We utilized the same RDKit features as in our other models, except for that the ClinTox model was an ensemble of five models and used the following optimal hyperparameters: message-passing steps = 6; neural network hidden size = 2200; number of feed-forward layers = 3; and dropout probability = 0.15. This ensemble of models was subsequently used to make toxicity predictions on our candidate molecules.

Chemical analyses

We utilized Tanimoto similarity to quantify the chemical relationship between molecules predicted in our study. The Tanimoto similarity of two molecules is a measure of the proportion of shared chemical substructures in the molecules. To compute Tanimoto similarity, we first determined Morgan fingerprints (computed using RDKit) for each molecule using a radius of 2 and 2048-bit fingerprint vectors. Tanimoto similarity was then computed as the number of chemical substructures contained in both molecules divided by the total number of unique chemical substructures in either molecule. The Tanimoto similarity is thus a number between 0 and 1, with 0 indicating least similar (no substructures are shared) and 1 indicating most similar (all substructures are shared). Morgan fingerprints with radius *R* and *B* bits are generated by looking at each atom and determining all of the substructures centered at that atom that include atoms up to *R* bonds away from the central atom. The presence or absence of these substructures is encoded as 1 and 0 in a vector of length *B*, which represents the fingerprint. For t-SNE analyses, plots were created using scikit-learn's implementation of t-Distributed Stochastic Neighbor Embedding. Here, we first used RDKit to compute Morgan fingerprints for each molecule using a radius of 2 and 2048-bit fingerprint vectors. We then used t-SNE with the Jaccard distance metric to reduce the data points from 2048 dimensions to the two dimensions that are plotted. Note that Jaccard distance is another name for Tanimoto distance, and Tanimoto distance is defined as: Tanimoto distance = 1 - Tanimoto similarity. Thus, the distance between points in the t-SNE plots is an indication of the Tanimoto similarity of the corresponding molecules, with greater distance between molecules indicating lower Tanimoto similarity. We used scikit-learn's default values for all t-SNE parameters besides the distance metric.

Chemical screening

E. coli BW25113 was grown overnight in 3 mL Luria-Bertani (LB) medium and diluted 1/10,000 into fresh LB. 99 μl of cells was added to each well of a 96-well flat-bottom plate (Corning) using a multichannel pipette. Next, 1 μl of a 5 mM stock of each molecule from an FDA-approved drug library supplemented with a natural product library (2,560 molecules total; MicroSource Discovery Systems) was added, in duplicate, using an Agilent Bravo liquid handler. The final screening concentration was 50 μM. Plates were then incubated in sealed plastic bags at 37°C without shaking for 16 hr, and subsequently read at 600 nm using a SpectraMax M3 plate reader (Molecular Devices) to quantify cell growth. Plate data were normalized based on the interquartile mean of each plate.

Growth inhibition assays

Cells were grown overnight in 3 mL LB medium and diluted 1/10,000 into fresh LB. In 96-well flat-bottom plates (Corning), cells were then introduced to compound at a final concentration of 50 μM, or to compound at two-fold serial dilutions, in final volumes of 100 μl. Plates were then incubated at 37°C without shaking until untreated control cultures reached stationary phase, at which time plates were read at 600 nm using a SpectraMax M3 plate reader. We note here that the incubation time required to reach stationary phase differed between species but was generally between 12 hr and 18 hr. For ZINC15 compound validation, the strains were *E. coli* BW25113, *S. aureus* USA 300, *K. pneumoniae* ATCC 700721, *A. baumannii* ATCC 17978, and *P. aeruginosa* PA01. *C. difficile* 630 growth inhibition was performed as described above, except cells were grown in BHI + 0.1% taurocholate for 18 hr in an anaerobic chamber (Coy Laboratory Products). *M. tuberculosis* H37Rv was grown at 37°C in Middlebrook 7H9 broth supplemented with 10% OADC (oleic acid-albumin-dextrose complex, vol/vol), 0.2% glycerol, and 0.05% Tween-80, or on Middlebrook 7H10 plates supplemented with 10% OADC and 0.5% glycerol. Cells were grown to mid-log phase, then added to 96-well plates at OD_{600} = 0.0025, in a total of 50 μl of 7H9 medium. In addition, each well contained 45 μl of 7H9 medium and varying compound concentrations diluted in a total of 5 μl of medium. Plates were incubated at 37°C in a humidified container for 14 days. OD_{600} was measured using a SpectraMax M5 plate reader.

Bacterial cell killing assays

Cells were grown overnight in 3 mL LB medium and diluted 1/10,000 into fresh LB. In 96-well flat-bottom plates (Corning), cells were grown to the required density, at which time antibiotic was added at the indicated concentration and cultures were incubated for the required duration. Cells were then pelleted in plates by centrifugation at 4000 x g for 15 min at 4°C and washed in ice cold PBS. After washing, cells were 10-fold serially diluted in PBS and plated on LB to quantify cell viability. In experiments where cells were incubated with antibiotic in nutrient-deplete conditions, cells were grown to the required density in LB media, washed in PBS, and subsequently resuspended in PBS prior to the addition of antibiotic. After cultures were incubated for the required duration, cells were pelleted in plates by centrifugation at 4000 x g for 15 min at 4°C and washed in ice cold PBS. After washing, cells were 10-fold serially diluted in PBS and plated on LB to quantify cell viability. *M. tuberculosis* M37Rv was grown to mid-log phase, then 30,000 cells were added to a 24 well plate in 1 mL of 7H9 medium. A sample from each well was taken as time = 0, prior to halicin addition, then halicin was added to each well at the 16 μg/ml (1x MIC). At the indicated time points, samples were taken from each well and plated on 7H10. Control wells contained the relevant DMSO concentration without halicin. Plates were incubated at 37°C and counted twice after 4 and 6 weeks.

Mutant generation

For serial passage evolution, *E. coli* BW25113 was grown overnight in 3 mL LB medium and diluted 1/10,000 into fresh LB. Cells were grown in 96-well flat-bottom plates (Corning), in the presence of varying concentrations of halicin (or ciprofloxacin) at two-fold serial dilutions, in final volumes of 100 μl. Plates were incubated at 37°C without shaking for 24 hr, at which time they were read at 600 nm using a SpectraMax M3 plate reader. After 24 hr, cells that grew in the presence of the highest concentration of halicin

(or ciprofloxacin) were diluted into fresh LB at the equivalent of 1/10,000 of a dense culture, and once again introduced to varying concentrations of halicin (or ciprofloxacin) at two-fold serial dilutions. This procedure was performed every 24 hr over the course of 30 days. For spontaneous suppressor generation, $\sim 10^9$ CFU of *E. coli* BW25113 grown in LB media was spread onto LB agar in 10 cm Petri dishes, either without antibiotics or supplemented with ciprofloxacin (Millipore Sigma) or halicin (TCI Chemicals) at the indicated concentrations. Plates were subsequently incubated at 37°C for seven days, at which time colonies from each plate were re-streaked onto LB and LB supplemented with antibiotics at the same concentration on which the colonies were originally grown. These plates were grown at 37°C overnight to monitor re-growth. For strain engineering, *E. coli* BW25113 *ΔnsfA*::kan *ΔnfsB*::cat was derived from BW25113 *ΔnsfA*::kan via introduction of a cat gene to disrupt the *nfsB* ORF using the Lambda Red method (Datsenko and Wanner, 2000). Briefly, 2 mL 2x YT media with BW25113 *ΔnsfA*::kan carrying the temperature-sensitive plasmid pKD46 at 30°C was induced with 20 mM arabinose. Upon reaching mid-log phase ($OD_{600} \sim 0.5$), cells were pelleted at 6000 x g for 2 min, then washed three times with 1 mL 15% glycerol. The final pellet was resuspended in 200 μl of 15% glycerol, and 50 μl was mixed with 300 ng of disruption fragment (generated using primers AB5044 and AB5045 on pKD32 to amplify the FRT-flanked cat cassette). Cells were electroporated at 1800 kV, then allowed to recover overnight in 5 mL 2x YT at 30°C. Cells were then pelleted at 6000 x g for 2 min, resuspended in 200 μl deionized water and plated on 2x YT agar plates with 15 μg/ml kanamycin (Millipore Sigma) and 20 μg/ml chloramphenicol (Millipore Sigma). Plates were incubated at 37°C for 24-48 hr. Single colonies were PCR checked (primers AB5046, AB5047) for loss of the *nfsB* gene (1069 bp) and appearance of the cat gene insertion (1472 bp). Finally, positive colonies were assayed for loss of pKD46 at 37°C by replica plating on 15 μg/ml kanamycin and 20 μg/ml chloramphenicol with or without 50 μg/ml carbenicillin (Millipore Sigma).

AB5044 TAGCCGGGCAGATGCCCGGCAAGAGAGAATTACACTTCGGTTAAGGTGATATTCCGGGGATCCGTCGACC
AB5045
ACCTTGTAATCTGCTGGCACGCAAAATTACTTTCACATGGAGTCTTTATGTGTAGGCTGGAGCTGCTTCG
AB5046
tgcaaaataatatgcaccacgacggcggtcagaaaaataa
AB5047
gaagcgttacttcgcgatctgatcaacgattcgtggaatc

RNA sequencing

Cells were grown overnight in 3 mL LB medium and diluted 1/10,000 into 50 mL fresh LB. When cultures reached $\sim 10^7$ CFU/ml, halicin was added at 0.25x MIC (0.5 μg/ml), 1x MIC (2 μg/ml), or 4x MIC (8 μg/ml) and cells were incubated for the noted durations. After incubation, cells were harvested via centrifugation at 15,000 x g for 3 min at 4°C, and RNA was purified using the Zymo Direct-zol 96-well RNA purification kit (R2056). Briefly, $\sim 10^7$-10^8 CFU pellets were lysed in 500 μl hot Trizol reagent (Life Technologies). 200 μl chloroform (Millipore Sigma) was added, and samples were centrifuged at 15,000 x g for 3 min at 4°C. 200 μl of the aqueous phase was added to 200 μl anhydrous ethanol (Millipore Sigma), and RNA was purified using a Zymo-spin plate as per the manufacturer's instructions. After purification, Illumina cDNA libraries were generated using a modified version of the RNAtag-seq protocol (Shishkin et al., 2015). Briefly, 500 ng – 1 μg of total RNA was fragmented, depleted of genomic DNA, dephosphorylated, and ligated to DNA adapters carrying 5′-AN_8-3′ barcodes of known sequence with a 5′ phosphate and a 3′ blocking group. Barcoded RNAs were pooled and depleted of rRNA using the RiboZero rRNA depletion kit (Epicenter). Pools of barcoded RNAs were converted to Illumina cDNA libraries in two main steps: (1) reverse transcription of the RNA using a primer designed to the constant region of the barcoded adaptor with addition of an adaptor to the 3′ end of the cDNA by template switching using SMARTScribe (Clontech), as previously described (Zhu et al., 2001); and (2) PCR amplification using primers whose 5′ ends target the constant regions of the 3′ or 5′ adaptors and whose 3′ ends contain the full Illumina P5 or P7 sequences. cDNA libraries were sequenced on the Illumina NextSeq 500 platform to generate paired end reads. Following sequencing, reads from each sample in a pool were demultiplexed based on their associated barcode sequence. Up to one mismatch in the barcode was allowed, provided it did not make assignment of the read to a different barcode possible. Barcode sequences were removed from the first read, as were terminal G's from the second read that may have been added by SMARTScribe during template switching. Next, reads were aligned to the *E. coli* MG1655 genome (NC_000913.3) using BWA (Li and Durbin, 2009) and read counts were assigned to genes and other genomic features. Differential expression analysis was conducted with DESeq2 (Love et al., 2014) and/or edgeR (Robinson et al., 2010). To verify coverage, visualization of raw sequencing data and coverage plots in the context of genome sequences and gene annotations was conducted using GenomeView (Abeel et al., 2012). To determine biological response of cells as a function of halicin exposure, we performed hierarchical clustering of the gene expression profiles using the *clustergram* function in MATLAB 2016a. We selected the Euclidean distance as the metric to define the pairwise distance between observations, which measures a straight-line distance between two points. The use of Euclidian distance has been considered as the most appropriate to cluster log-ratio data (D'haeseleer, 2005). With a metric defined, we next selected the average linkage as the clustering method. The average linkage uses the algorithm called unweighted pair group method with arithmetic mean (UPGMA), which is the most popular and preferred algorithm for hierarchical data clustering (Jaskowiak et al., 2014; Loewenstein et al., 2008). UPGMA uses the mean similarity across all cluster data points to combine the nearest two clusters into a higher-level cluster. UPGMA assumes there is a constant rate of change among species

(genes) analyzed. We tested all alternative clustering metrics available (i.e., Spearman, Hamming, cosine, etc.) in the *pdist* function within the *clustergram* function in MATLAB and concluded that the Euclidean metric together with the average linkage allow the clearest and probably most meaningful definition of clusters for our dataset. Transcript cluster enrichment was performed using EcoCyc Pathway Tools (Karp, 2001; Karp et al., 2016; Keseler et al., 2013). *P value*s were calculated using Fisher's exact test.

$DiSC_3(5)$ assays

S. aureus USA300 and *E. coli* MC1061 were streaked onto LB agar and grown overnight at 37°C. Single colonies were picked and used to inoculate 50 mL LB in 250 mL baffled flasks, which were incubated for 3.5 hr in a 37°C incubator shaking at 250 rpm. Cultures were pelleted at 4000 x g for 15 min and washed three times in buffer. For *E. coli*, the buffer was 5 mM HEPES with 20 mM glucose (pH 7.2). For *S. aureus*, the buffer was 50 mM HEPES with 300 mM KCl and 0.1% glucose (pH 7.2). Both cell densities were normalized to OD_{600}~0.1, loaded with 1 μM $DiSC_3(5)$ dye (3,3′-dipropylthiadicarbocyanine iodide), and left to rest for 10 min in the dark for probe fluorescence to stabilize. Fluorescence was measured in a cuvette-based fluorometer with stirring (Photon Technology International) at 620 nm excitation and 670 nm emission wavelengths. A time-course acquisition was performed, with compounds injected after 60 s of equilibration to measure increases or decreases in fluorescence. For *E. coli*, polymyxin B was used as a control to monitor $\Delta\psi$ dissipation. For *S. aureus*, valinomycin was used as a $\Delta\psi$ control and nigiricin was used as a ΔpH control. Upon addition of antibiotic, fluorescence was read continuously for 3 min and at an endpoint of 4 hr.

EXPERIMENTAL MODEL AND SUBJECT DETAILS

baumannii mouse infection model

Experiments were conducted according to guidelines set by the Canadian Council on Animal Care, using protocols approved by the Animal Review Ethics Board at McMaster University under Animal Use Protocol #17-03-10. Before infection, mice were relocated at random from a housing cage to treatment or control cages. No animals were excluded from analyses, and blinding was considered unnecessary. Six- to eight-week old BALB/c mice were pretreated with 150 mg/kg (day −4) and 100 mg/kg (day −1) of cyclophosphamide to render mice neutropenic. Mice were then anesthetized using isofluorane and administered the analgesic buprenorphine (0.1 mg/kg) intraperitoneally. A 2 cm^2 abrasion on the dorsal surface of the mouse was inflicted through tape-stripping to the basal layer of epidermis using approximately 25-30 pieces of autoclave tape. Mice were infected with ~$2.5x10^5$ CFU *A. baumannii* CDC 288 directly pipetted on the wounded skin. The infection was established for 1 hr prior to treatment with Glaxal Base supplemented with vehicle (0.5% DMSO) or halicin (0.5% w/v). Groups of mice were treated 1 hr, 4 hr, 8 hr, 12 hr, 20 hr, and 24 hr post-infection. Mice were euthanized at the experimental endpoint of 25 hr and the wounded tissue collected, homogenized, and plated onto LB to quantify bacterial load.

C. difficile mouse infection model

Experiments were conducted according to protocol IS00000852-3, approved by Harvard Medical School Institutional Animal Care and Use Committee and the Committee on Microbiological Safety. *C. difficile* 630 spores were prepared from a single batch and stored long term at 4°C, as previously reported (Edwards and McBride, 2016). To disrupt colonization resistance and enable infection with *C. difficile*, four colonies (n = 20) of six- to eight-week-old C57BL/6 mice were administered 200 mg/kg ampicillin every 24 hr for 72 hr via intraperitoneal injection. Antibiotic-treated mice were given 24 hr to recover prior to infection with *C. difficile*. A total of $5x10^3$ spores of *C. difficile* strain 630 was delivered via oral gavage and mice were randomly assigned to three treatment groups: 50mg/kg metronidazole (n = 7), 15 mg/kg halicin (n = 7) and 10% PEG 300 vehicle (n = 6). We note here that three mice from the halicin treatment group failed to display *C. difficile* colonization. Beginning at 24 hr after *C. difficile* challenge, mice were gavaged with antibiotics or vehicle control every 24 hr for five days. To monitor *C. difficile* colonization, fecal samples were collected, weighed and diluted under anaerobic conditions with anaerobic PBS. CFUs were quantified using TCCFA plates supplemented with 50 μg/ml erythromycin at 37°C under anaerobic conditions, as previously described (Winston et al., 2016).

DATA AND CODE AVAILABILITY

Code availability

Chemprop code is available at: https://github.com/swansonk14/chemprop.

RNA sequencing data

RNA sequencing data is available at the NCBI Sequence Read Archive under accession PRJNA598708.

ADDITIONAL RESOURCES

Online model availability

A web-based version of the antibiotic prediction model described herein is available at: http://chemprop.csail.mit.edu/.

Cell

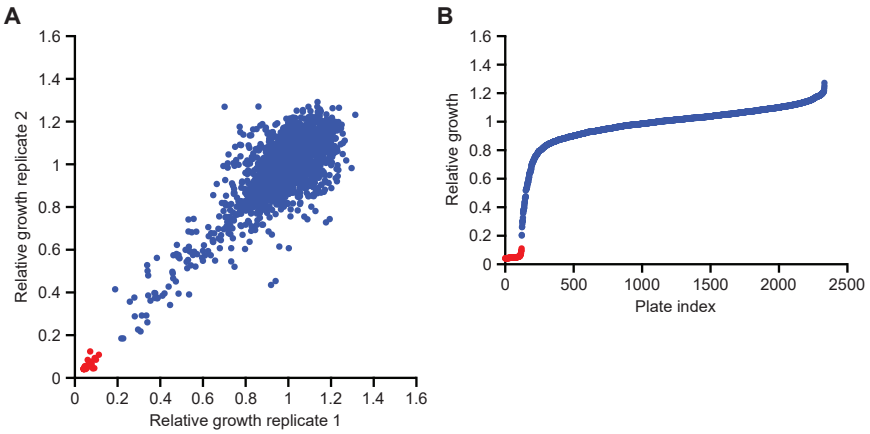

Figure S1. Primary Screening and Initial Model Training, Related to Figure 2.

(A) Primary screening data for growth inhibition of *E. coli* by 2,560 molecules within the FDA-approved drug library supplemented with a natural product collection. Red are growth inhibitory molecules; blue are non-growth inhibitory molecules. (B) Rank-ordered de-duplicated screening data containing 2,335 molecules. Shown is the mean of two biological replicates. Red are growth inhibitory molecules; blue are non-growth inhibitory molecules.

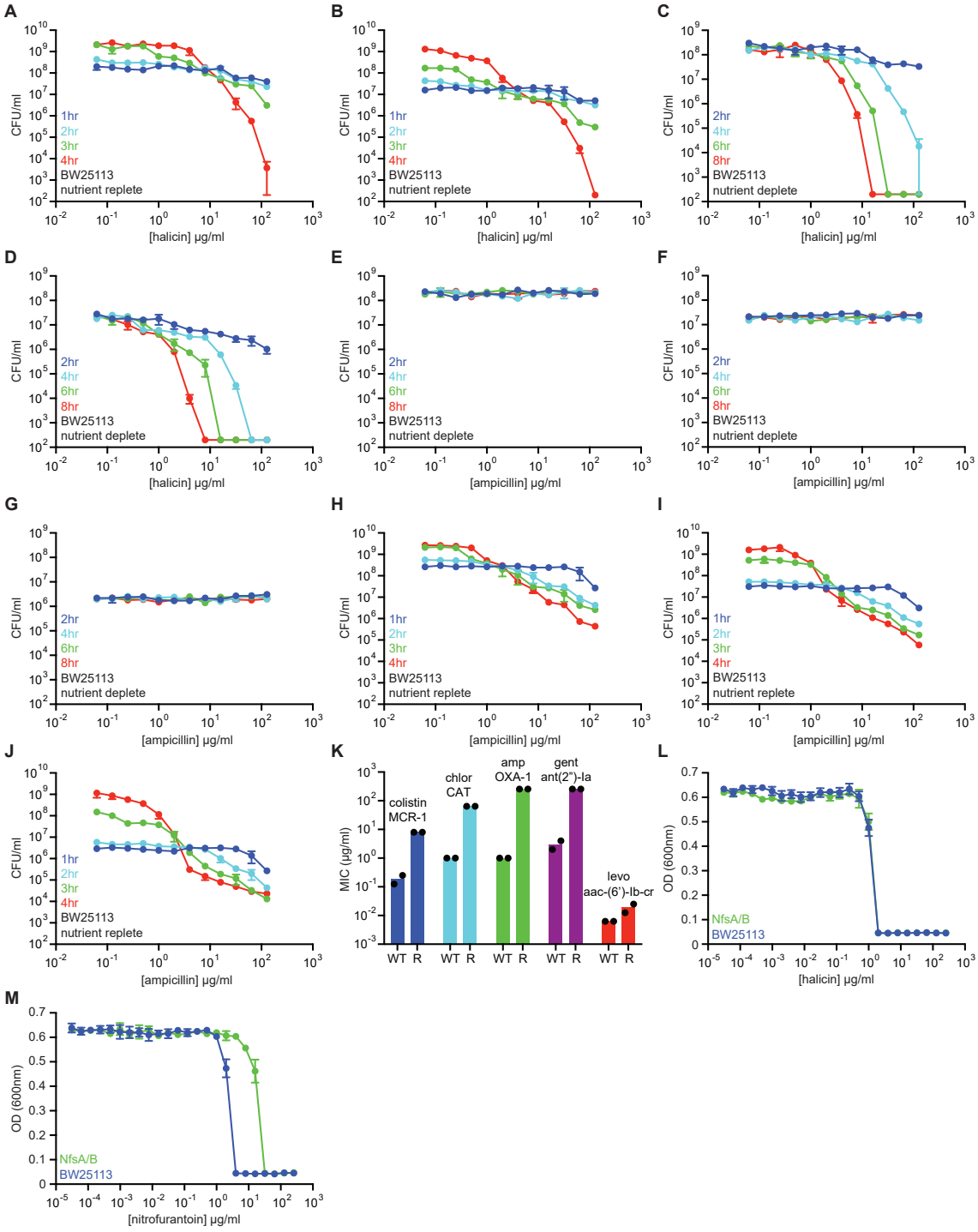

Figure S2. Activity of Halicin, Related to Figure 3

(A) Killing of *E. coli* in LB media in the presence of varying concentrations of halicin after 1 hr (blue), 2 hr (cyan), 3 hr (green), and 4 hr (red). The initial cell density is ~10^8 CFU/ml. Shown is the mean of two biological replicates. Bars denote absolute error. (B) Same as (A), with initial cell density ~10^7 CFU/ml. (C) Killing of *E. coli* in PBS in the presence of varying concentrations of halicin after 2 hr (blue), 4 hr (cyan), 6 hr (green), and 8 hr (red). The initial cell density is ~10^8 CFU/ml. Shown is the mean of two biological replicates. Bars denote absolute error. (D) Same as (C), with initial cell density ~10^7 CFU/ml. (E) Killing of *E. coli* in PBS in the presence of varying concentrations of ampicillin after 2 hr (blue), 4 hr (cyan), 6 hr (green), and 8 hr (red). The initial cell density is ~10^8 CFU/ml. Shown is the mean of two biological replicates. Bars denote absolute error. (F) Same as (E), with initial cell density ~10^7 CFU/ml. (G) Same as (E), with initial cell density ~10^6 CFU/ml. (H) Killing of *E. coli* in LB media in the presence of varying concentrations of ampicillin after 1hr (blue), 2 hr (cyan), 3 hr (green), and 4 hr (red). The initial cell density is ~10^8 CFU/ml. Shown is the mean of two biological replicates. Bars denote absolute error. (I) Same as (H), except with initial cell density ~10^7 CFU/ml. (J) Same as

(legend continued on next page)

(H), except with initial cell density $\sim 10^6$ CFU/ml. (K) MIC of various antibiotics against *E. coli* strains harboring a range of plasmid-borne, functionally diverse, antibiotic-resistance determinants. The *mcr-1* gene was expressed in *E. coli* BW25113. All other resistance genes were expressed in *E. coli* BW25113 *ΔbamBΔtolC*. WT is wild-type *E. coli*. R is *E. coli* harboring a resistance plasmid. Chlor is chloramphenicol. Amp is ampicillin. Gent is gentamicin. Levo is levofloxacin. Experiments were conducted with two biological replicates. (L) Growth inhibition of wild-type *E. coli* (blue) and *ΔnfsAΔnfsB E. coli* (green) by halicin. Shown is the mean of two biological replicates. Bars denote absolute error. (M) Growth inhibition of wild-type *E. coli* (blue) and *ΔnfsAΔnfsB E. coli* (green) by nitrofurantoin. Shown is the mean of two biological replicates. Bars denote absolute error.

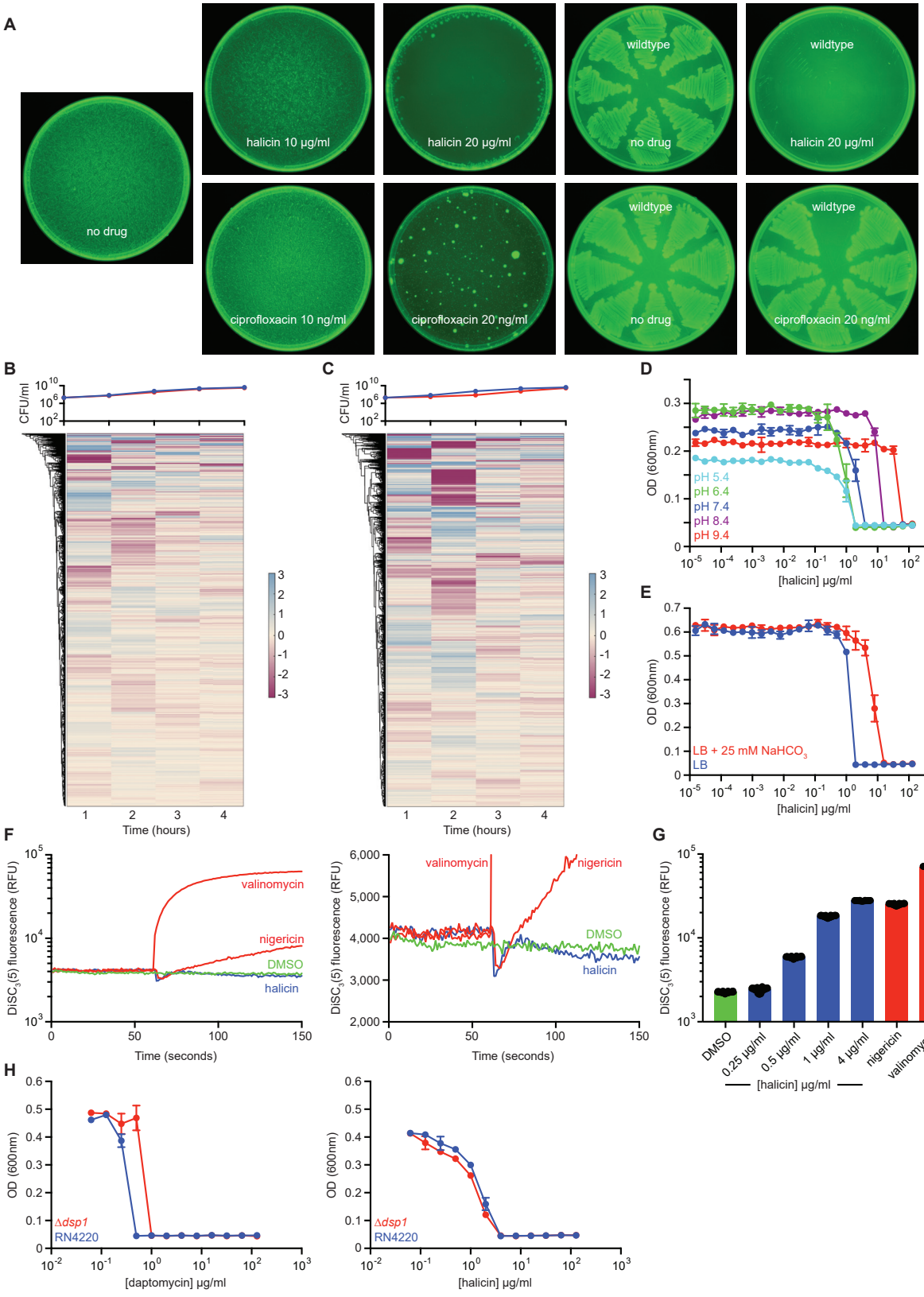

(legend on next page)

Figure S3. Mechanistic Investigations into Halicin, Related to Figure 4

(A) Evolution of spontaneous resistance against halicin (top) or ciprofloxacin (bottom). *E. coli* BW25113 ($\sim 10^9$ CFU) was plated onto non-selective or selective media and incubated for 7 days prior to imaging, and re-streaking of colonies onto fresh non-selective or selective media. 20 μg/ml halicin and 20 ng/ml ciprofloxacin, respectively, were used for suppressor mutant evolution. Note that the colonies that emerged at the edge of halicin-supplemented plates after 7 days grew well on LB non-selective media but did not re-streak onto halicin-supplemented media. All seven selected ciprofloxacin-resistant colonies grew on both non-selective and ciprofloxacin-supplemented media. (B) Whole transcriptome hierarchical clustering of *E. coli* treated with halicin at 0.25x MIC for 1hr, 2 hr, 3 hr, and 4 hr. Shown is the mean transcript abundance of two biological replicates of halicin-treated cells relative to untreated control cells on a $\log_2$-fold scale. In the growth curve, blue represents untreated cells; red represents halicin-treated cells. (C) Same as (B), except cells were treated with 1x MIC halicin. (D) Growth inhibition by halicin against *S. aureus* USA300 in pH-adjusted media. Shown is the mean of two biological replicates. Bars denote absolute error. (E) Growth inhibition by halicin against *E. coli* in LB (blue) or LB supplemented with 25 mM sodium bicarbonate (red), which dissipates the ΔpH component of the proton motive force. Shown is the mean of two biological replicates. Bars denote absolute error. (F) $DiSC_3(5)$ fluorescence in *S. aureus* upon exposure to valinomycin (64 μg/ml; dissipates $\Delta\psi$), nigericin (16 μg/ml; dissipates ΔpH), halicin (4 μg/ml), or DMSO. Halicin induced fluorescence changes more similar to nigericin relative to valinomycin, suggesting that halicin dissipates the ΔpH component of the proton motive force. The right panel is a magnified image of the drug-induced decrease in fluorescence shown in the left. (G) $DiSC_3(5)$ fluorescence in *S. aureus* upon exposure to valinomycin, nigericin, halicin, or DMSO after 4 hr of exposure. (H) Growth inhibition by daptomycin (left) and halicin (right) against *S. aureus* RN4220 (blue) or a daptomycin-resistant RN4220 strain (Δ*dsp1*; red) in LB media. Shown is the mean of two biological replicates. Bars denote absolute error.

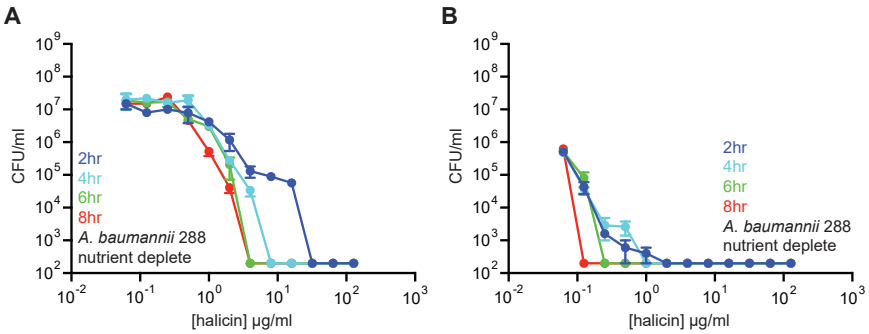

Figure S4. Activity of Halicin against *A. baumannii* CDC 288, Related to Figure 5

(A) Killing of *A. baumannii* in PBS in the presence of varying concentrations of halicin after 2 hr (blue), 4 hr (cyan), 6 hr (green), and 8 hr (red). The initial cell density is $\sim 10^7$ CFU/ml. Shown is the mean of two biological replicates. Bars denote absolute error. (B) Same as (A), with initial cell density $\sim 10^6$ CFU/ml.

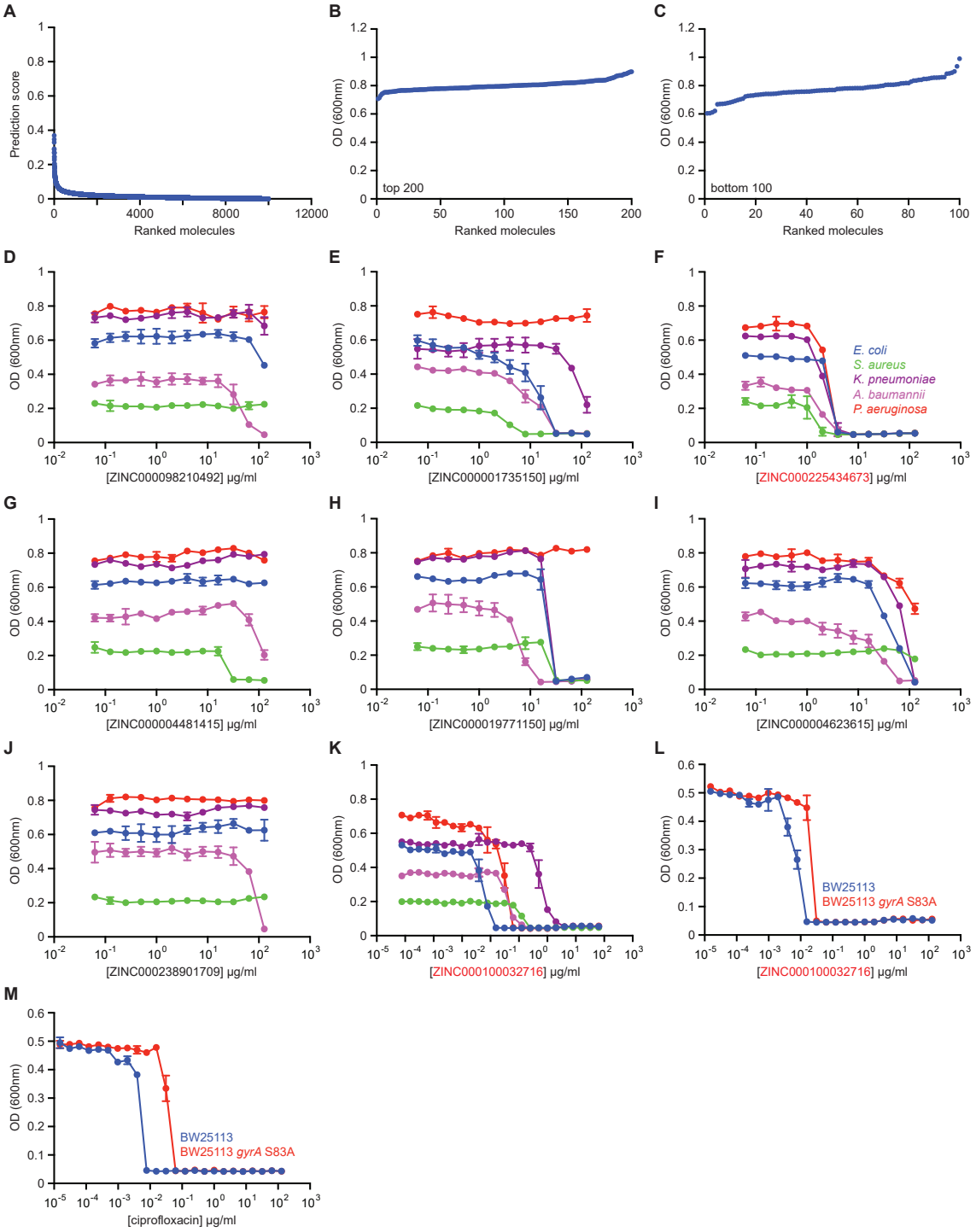

Figure S5. Model Predictions from the WuXi Anti-tuberculosis Library and the ZINC15 Database, Related to Figure 6

(A) Rank-ordered prediction scores of WuXi anti-tuberculosis library molecules. Note the overall low prediction scores. (B) The top 200 predictions from the data shown in (A) were curated for empirical testing for growth inhibition of *E. coli*. None were growth inhibitory, in agreement with their low prediction scores. Shown is the mean of two biological replicates. (C) The bottom 100 predictions from the data shown in (A) were curated for empirical testing for growth inhibition of *E. coli*. None were growth inhibitory, in agreement with their low prediction scores. Shown is the mean of two biological replicates. (D-K) Growth inhibition by eight empirically validated ZINC15 predictions against *E. coli* (blue), *S. aureus* (green), *K. pneumoniae* (purple), *A. baumannii* (pink), and *P. aeruginosa* (red) in LB media. Shown is the mean of two biological replicates. Bars denote absolute error. (L) Growth inhibition by ZINC000100032716 against *E. coli* BW25113 (blue) or a ciprofloxacin-resistant *gyrA* S83A mutant of BW25113 (red). Shown is the mean of two biological replicates. Bars denote absolute error. (M) Same as (L) except using ciprofloxacin. Note the 4-fold smaller change in MIC with ZINC000100032716 between the *gyrA* mutant and wild-type *E. coli* relative to ciprofloxacin.